
Commissioning Of The Air Shower Fluorescence Telescope Prototype FAMOUS

von

Franziska Hanna Knuth

Bachelorarbeit in Physik

vorgelegt der
Fakultät für Mathematik, Informatik und Naturwissenschaften
der
Rheinisch-Westfälischen Technischen Hochschule Aachen

im Juli 2014

angefertigt am

III. Physikalischen Institut A

betreut durch

Univ.-Prof Thomas Hebbeker

Erstgutachter und Betreuer

Prof. Dr. Thomas Hebbeker
III. Physikalisches Institut A
RWTH Aachen University

Zweitgutachter

Prof. Dr. Christopher Wiebusch
III. Physikalisches Institut B
RWTH Aachen University

Abstract

The FAMOUS telescope prototype has been developed for the observation of fluorescence light emitted in air showers which are introduced by ultra high energy cosmic rays. It is based on silicon photomultipliers as detector component. In this thesis, the commissioning of the telescope has been performed. The SkyCam module has been implemented, which enables the monitoring of the night sky and the detection of visible stars. The determination of the breakdown voltage of the silicon photomultipliers and other calibrations for the data acquisition and the optics have been accomplished. Beside this, several measurements have been performed to test the current prototype.

Auszug

Das FAMOUS Teleskop ist entwickelt für die Beobachtung von dem bei Luftschauern emittierten Fluoreszenz Licht, welche von höchst energetischen kosmischen Teilchen ausgelöst werden. Das Teleskop basiert auf Siliziumphotodetektoren als aktive Komponente. Im Rahmen dieser Arbeit wurde das FAMOUS Teleskop in Betrieb genommen. Das SkyCam Modul wurde entwickelt, das die Beobachtung des Nachthimmels, sowie die Zuordnung sichtbarer Sterne ermöglicht. Neben der Bestimmung der Durchbruchspannung der Siliziumphotodetektoren wurden weitere Kalibrierungen für das Daten verarbeitende System und die Optik durchgeführt. Außerdem wurden des Teleskop in ersten nächtlichen Messungen erprobt.

Contents

| | | |
|----------|--|-----------|
| 1 | Introduction | 1 |
| 2 | Cosmic rays | 2 |
| 2.1 | The energy spectrum of high energy cosmic rays | 2 |
| 2.2 | Extensive air showers | 3 |
| 2.3 | The Fluorescence light detection technique | 5 |
| 2.4 | The Pierre Auger Observatory | 7 |
| 3 | FAMOUS | 9 |
| 3.1 | Silicon photomultipliers | 9 |
| 3.2 | The telescope prototype FAMOUS | 12 |
| 3.2.1 | The baseline design | 12 |
| 3.2.2 | The data acquisition system | 14 |
| 3.2.3 | The slow control interface | 15 |
| 4 | The SkyCam night sky camera | 17 |
| 4.1 | Correction of the image distortion | 17 |
| 4.1.1 | General approach | 17 |
| 4.1.2 | Experimental setup | 19 |
| 4.1.3 | Results | 20 |
| 4.2 | Detection of visible stars | 22 |
| 4.2.1 | Astrometry | 22 |
| 4.2.2 | Operating principle | 23 |
| 5 | Commissioning of FAMOUS | 26 |
| 5.1 | Determination of the break down voltage of SiPMs | 26 |
| 5.1.1 | Finger spectrum method | 26 |
| 5.1.2 | Gradient of the QDC signal | 29 |
| 5.1.3 | Result and comparison of the different methods | 30 |
| 5.2 | Calibration of the QDC pedestal | 31 |
| 5.3 | Focusing of the FAMOUS camera | 32 |

| | | |
|----------|---|-----------|
| 6 | Measurements | 33 |
| 6.1 | Discovered necessary improvements | 33 |
| 6.2 | Measurements during dawn | 34 |
| 6.3 | Night sky brightness | 34 |
| 6.4 | Traces of celestial objects | 36 |
| 6.4.1 | Trace of the moon | 36 |
| 6.4.2 | Traces of stars | 38 |
| 7 | Summary and Outlook | 40 |
| | References | 44 |
| | Acknowledgements | 45 |

Introduction

The Pierre Auger Observatory located in Argentina is the World's largest observatory for cosmic rays. There the arrival of extensive air showers, caused by primary cosmic rays, are studied, by use of a hybrid detector. This is composed of a surface and a fluorescence detector, which consists of 27 optical telescopes. The camera of the fluorescence telescope is constructed with photomultiplier tubes (PMTs).

In this thesis, the FAMOUS telescope prototype is studied (c.f. 1.1). It is based on silicon photomultipliers (SiPMs), which are promising replacements for the widely used PMTs.

The characteristics of the SiPM, such as gain and noise phenomena, are defined by the over voltage, which is the difference between bias and breakdown voltage. Multiple methods to determine the breakdown voltage have been developed and are presented in this thesis.

The current version of the FAMOUS telescope has seven pixels, where the upgrading to a 64-pixel-version is planned for the near future.

Within the commissioning, the SiPMs pedestal is calibrated and the focusing of SiPM camera is brought forward.

Further more, the SkyCam module for the observation of the night sky has been implemented. The basis of the SkyCam is an CMOS camera combined with a wide angle lens. A method for the correction of the image distortion has been developed. The SkyCam module enables the detection of visible stars with help of the Astrometry.net software.

To test the current prototype of FAMOUS, several nightly measurement have been performed, to identify weak points and develop possible improvements. In connection to this, the night sky has been observed and traces of celestial objects have been recorded.

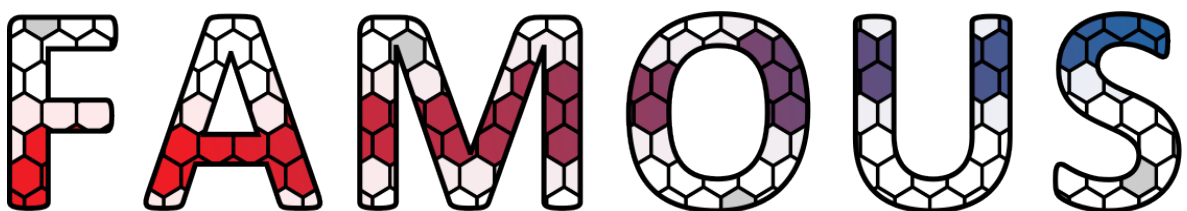


Figure 1.1: The logo of FAMOUS. The acronym stands for „First Auger Multi-pixel photon counter camera for the Observation of Ultra-high-energy air Showers“. Taken from [1].

Cosmic rays

Through Victor Hess's balloon flight in 1912, a new window to the cosmos has been opened. Hess found that the ionizing radiation increases with increasing altitude [2]. Thus, the origin of this radiation could not be radioactive materials in the Earth. Instead, the source must be searched in the outer space. This discovery was the origin of additional research, which was done among others by Pierre Auger. He measured the arrival of ionized particles in coincidence using Geiger-Müller tubes and Wilson chambers, separated by a large distance up to 300 m [3]. He concluded that the measured particles are secondary particles generated by a primary cosmic ray interacting with the atmosphere.

In this chapter, some essential facts about the energy spectrum of the primary cosmic rays and the shower of secondary particles, referred to as extensive air shower are presented. Furthermore, the detection of fluorescence light and the Pierre Auger Observatory are introduced.

2.1 The energy spectrum of high energy cosmic rays

The flux of cosmic rays has been measured directly by various experiments with detectors at the edge and above the atmosphere [2]. For example with hydrogen-filled balloons up to heights of 9 km [2] or by satellite based experiments like PAMELA [4]. As well, it has been measured indirectly with large ground based detectors observing the secondary particles produced by interactions of the cosmic ray with molecules of the air.

In figure 2.1, it can be seen that the flux decreases dramatically with higher energies. The flux of particles with an energy of 10^{20} eV corresponds to only one particle per square kilometre and century [2]. For energies above 10^{11} eV, the flux follows a steeply falling power law $dN/dE \propto E^{-\gamma}$ [2]. The spectral index γ is constant for wide energy ranges, but changes at distinctive points. Starting at lower energies, γ is approximately -2.7 and changes to -3.1 by an energy of about $4 \cdot 10^{15}$ eV. This structure is referred to as the knee. It is followed by the second knee approximately at $4 \cdot 10^{17}$ eV and the ankle at circa $5 \cdot 10^{18}$ eV [6], where γ changes to -2.6 [2]. At about $4 \cdot 10^{19}$ eV, a strong flux suppression can be observed. The origins of these structures are much discussed. A common explanation is transition to other origins and mechanisms of the acceleration. For example the knee marks the change from galactic to extragalactic accelerators. The flux suppression at the highest energies can be explained both by the interaction of the cosmic rays with the cosmic microwave background, referred to as GZK-Cutoff (Greisen-Zatsepin-Kuzmin Cutoff), as by reaching the end of acceleration methods [6]. The structure of the energy spectrum is discussed in much more detail in [7].

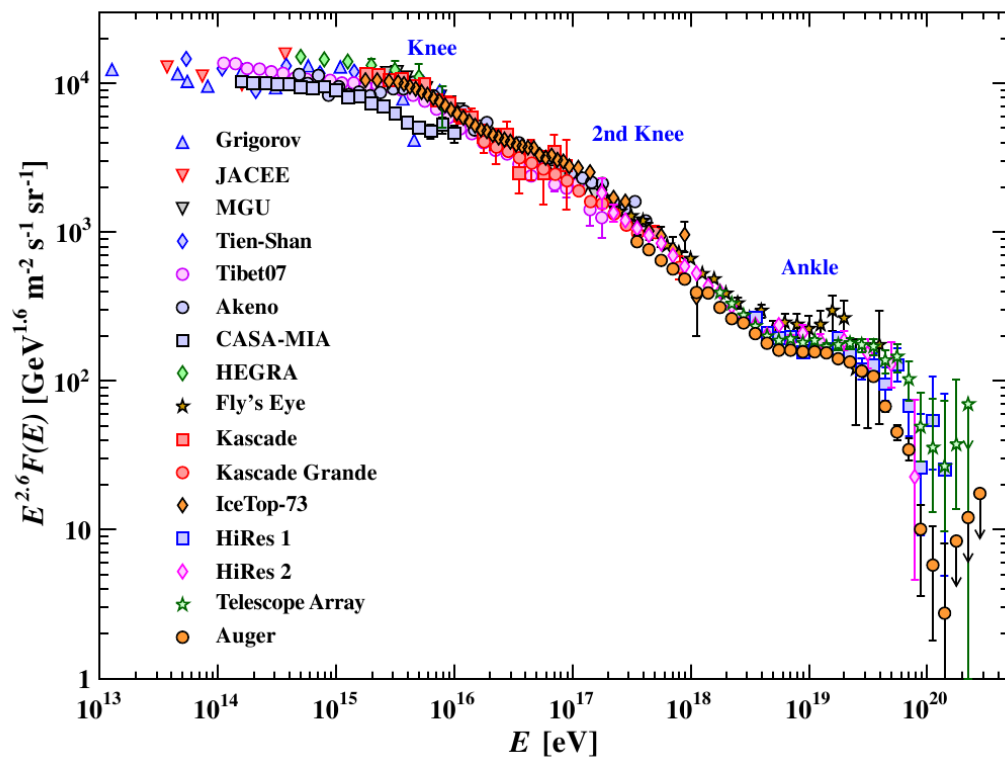


Figure 2.1: Cosmic ray flux for all particles as a function of energy containing data from several experiments. To reveal the structure, the flux is multiplied by $E^{2.6}$. Taken from [5].

When discussing the spectrum, also the question to the chemical composition occurs, because the all particle spectrum (c.f. figure 2.1) does not allow to draw conclusion about the origins of the cosmic rays [6]. At lower energies, the chemical composition has already been measured [5]. At the highest energies, the chemical composition is still under investigation and currently a great field of research.

2.2 Extensive air showers

When a primary cosmic ray enters the atmosphere of the Earth it interacts with the air molecules, for example oxygen or nitrogen [2]. Due to this interaction, various secondary particles are produced. These secondaries interact with the air molecules or decay, creating a shower of secondaries. As presented in figure 2.2, the shower consists of three main components, namely the electromagnetic, the hadronic and the muonic component, which also contains neutrinos [8]. Studying the rates of the components, drawing inferences to the chemical compound of the primary becomes possible.

Is a shower induced by an electron or photon, it is referred to as electromagnetic shower [5]. Since the main production processes in this type of shower are bremsstrahlung and pair production, the muonic component is rather small. To understand the main properties of an electromagnetic shower, the Heitler model can be used (c.f. [9]).

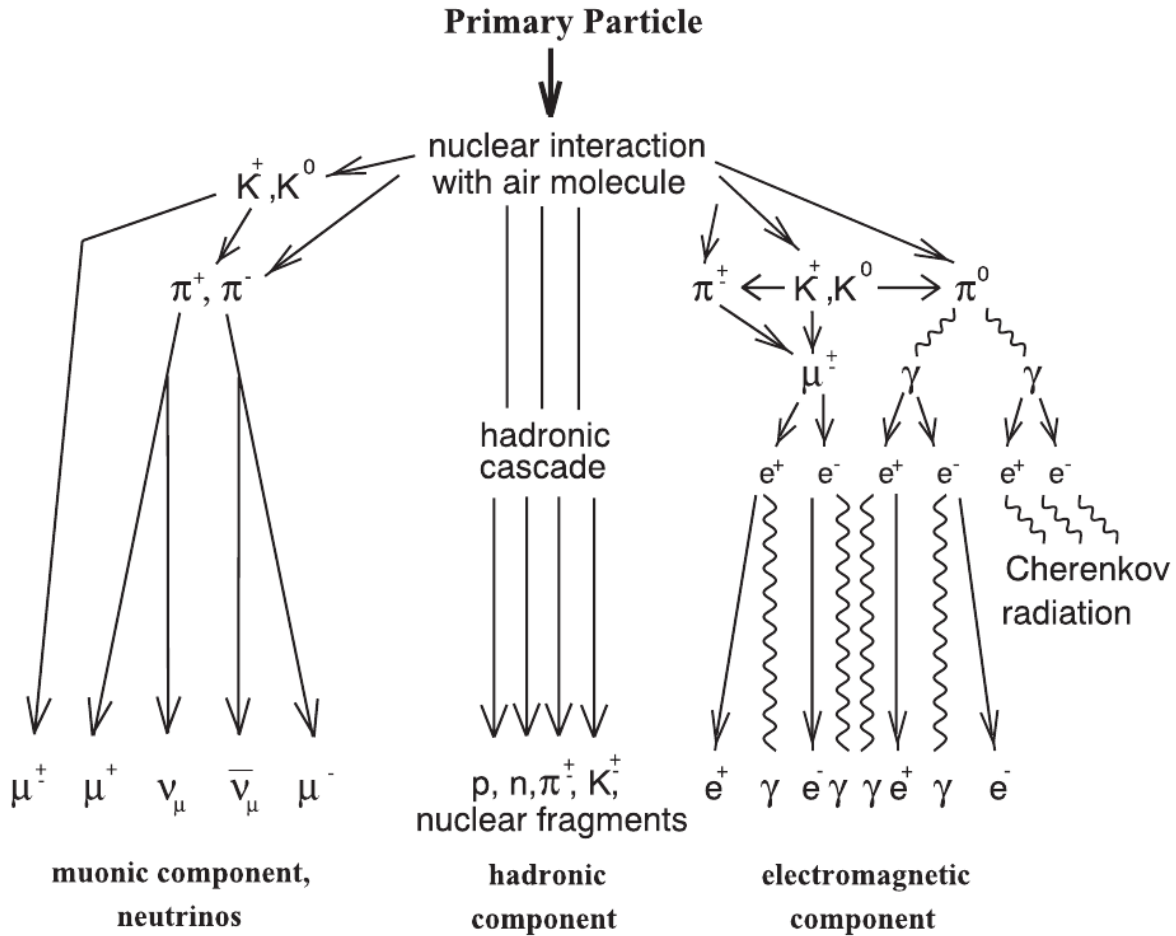


Figure 2.2: Schematic development of an extensive air shower, outlining the three components created in the shower. Taken from [8].

In contrast to an electromagnetic shower, a hadron-initiated shower develops a significant muonic component. Furthermore, a large event to event fluctuation can be observed for this type of shower [2].

The shape of the shower consists of a thin disc, which travels to ground with nearly the speed of light [2]. The disc thickness is in the order of meters, whereas the disc extends in the order of kilometers. To describe the longitudinal shower profile of an extensive air shower, the Gaisser-Hillas function can be used [10]:

$$f_{\text{GH}}(X) = w_{\text{max}} \left(\frac{X - X_0}{X_{\text{max}} - X_0} \right)^{\frac{X_{\text{max}} - X_0}{\Lambda}} \exp \left(- \frac{X_{\text{max}} - X}{\Lambda} \right). \quad (2.1)$$

In this formula X_{max} represents the depth of the shower maximum, at which the maximum energy deposit w_{max} is reached [10]. X_0 and Λ are shape parameters. Here, X_{max} and X are measured in units of gram per square centimetre, as they are representing the amount of traversed matter. This quantity has the advantage that it is independent from the entry angle into the atmosphere.

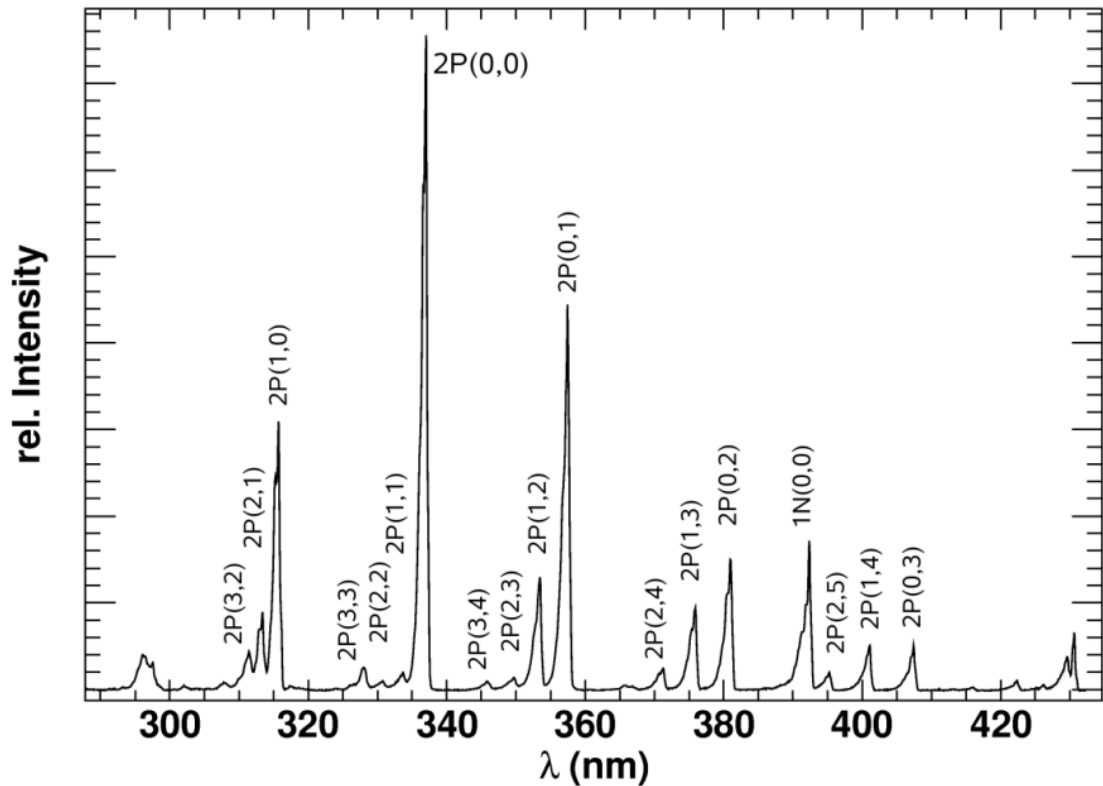


Figure 2.3: Fluorescence light spectrum of dry air at 800 hPa and 20 °C, measured by the AIRFLY experiment. The labeling of the spectrum includes the exited state (1N or 2P) and the change of the vibration quantum number (ν' , ν''). Taken from [2].

To measure the longitudinal profile, the fluorescence light originated in the excitation of nitrogen molecules can be used. As soon as the profile is known, the energy of the primary can be reconstructed. This principle is described in the next section.

2.3 The Fluorescence light detection technique

Due to the development of an extensive air shower, the charged component of the shower excites nitrogen molecules in the air [11]. Induced by the relaxation, fluorescence light is emitted isotropically. An example of a measured spectrum can be found in figure 2.3, characterized by multiple rotation and vibration states. The spectrum covers mainly the wavelengths from 300 to 400 nm, near the ultraviolet domain.

The aim of observing the emitted fluorescence light is its dependency of the energy deposit [2]. The number of photons produced by the shower is proportional to the energy deposit dE/dX [12]:

$$\frac{d^2N_\gamma}{dXd\lambda} = Y(\lambda, T, p, u) \cdot \frac{dE}{dX} . \quad (2.2)$$

In this formula, N_γ is the number photons and $Y(\lambda, T, p, e)$ the fluorescence yield. It depends on the wavelength λ of the photon and atmospheric conditions as temperature

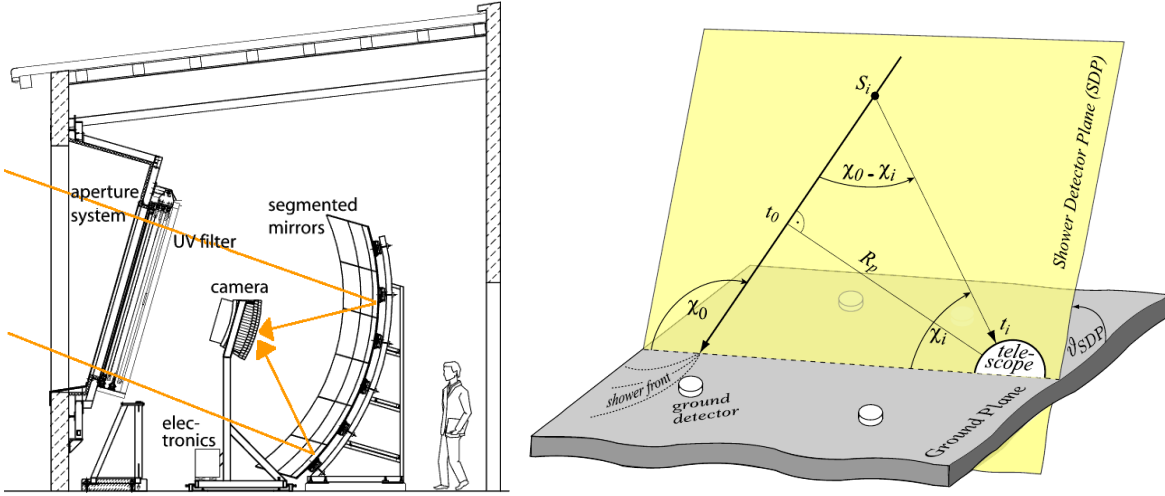


Figure 2.4: Left: schematic plan of the fluorescence telescope of the Pierre Auger Observatory. Right: Illustration of the geometrical shower reconstruction from the observables of the fluorescence detector exemplified at the Pierre Auger Observatory. Adapted from [11].

T, pressure p and humidity u . As Y is only slightly dependent on its parameters and is approximately five photons per MeV of deposited Energy.

Thus, the integrated shower profile results in nearly the whole shower energy [2]. The missing energy is conditionally to particles not exiting nitrogen molecules like neutrinos. For example, a primary with $E = 10^{19}$ eV has missing energy of approximately ten percent. Monte Carlo simulations have to be used to corrected the measured data for the missing energy.

Hence the number of photons as function of the slant depth has to be measured. A possible measurement setup as used at the Pierre Auger Observatory is shown in figure 2.4. Via the segmented mirror, the fluorescence light is reflected to the pixel camera containing 440 photomultipliers each with a field of view of approximately 1.5° [11].

The observation of an extensive air shower can be performed either in monocular or in stereo observation, differing if the shower is registered by one or more telescopes [11]. The advantage of multiple cameras observing the shower is an improved angular resolution, and a preciser determination of the energy deposit. In this case, the shower axis is calculated from the intersection of the shower planes observed by the individual telescopes. If only one telescope detects the shower, the timing information of each pixel t_i has to be used to reconstruct the shower axis:

$$t_i = t_0 + \frac{R_p}{c} \tan \left(\frac{\chi_0 - \chi_i}{2} \right) . \quad (2.3)$$

As illustrated in figure 2.4, t_0 is the time of the least distance R_p , χ_0 is the angle between the track and the horizontal plane and χ_i denotes the angle between the direction of view of the pixel and the horizontal.

Once the geometrical shower profile is known, the measured signal can be transferred to the number of detected photons and further the number of originated photons in

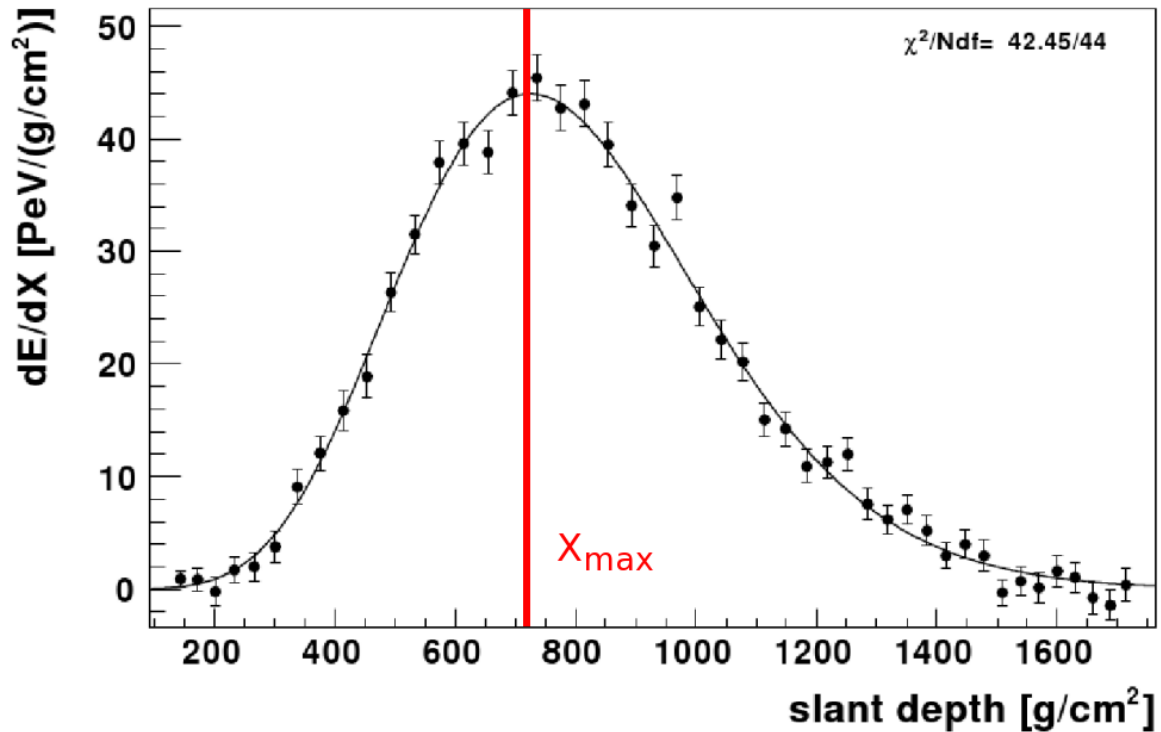


Figure 2.5: Longitudinal profile of energy deposit as a function of the slant depth with fitted Gaisser-Hillas function. Adapted from [11].

the extensive air shower can be reconstructed [11]. By use of equation 2.2 the energy deposit per slant depth can be reconstructed. The data of one measurement of the Pierre Auger Observatory, together with an fitted Gaisser-Hillas function can be seen in 2.5.

2.4 The Pierre Auger Observatory

The Pierre Auger Observatory is located in the Pampa Amarilla, Argentina. It is the World's largest observatory for the observation of ultra high energy cosmic rays. Since 2008, it is collecting data using a hybrid technology, composed of a surface and a fluorescence detector. A map of the observatory is shown in figure 2.6.

The surface detector consists of a triangular grid of 1,600 stations with a spacing of 1.5 km covering an area of 3000 km². Each station comprises a hight tight tank filled with twelve tons of pure water. When a charged particle passes through the tank Cherenkov light is produced. These signals are read out using three 9" photomultiplier-tubes. The duty cycle of the surface detector is close to 100 % [14].

The surface detector is overlooked by five telescope buildings housing 27 fluorescence detectors as seen in figure 2.4. Thus each telescope has an azimuth field of view of 30°, one telescope building overlooks 180° in azimuth and 28.6° in elevation. Attributable to the properties of the photomultiplier-tubes and the faint fluorescence light signal,

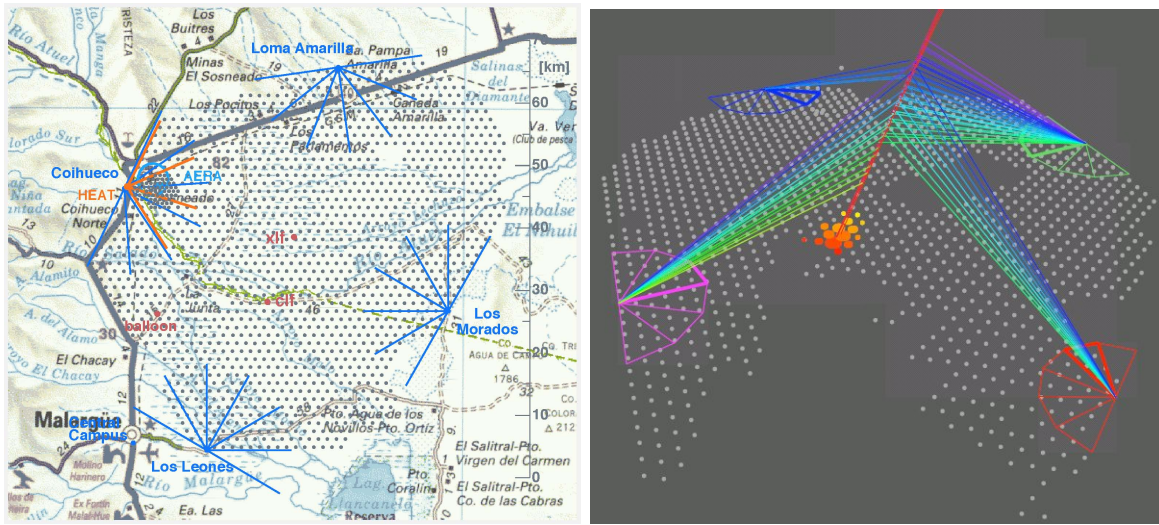


Figure 2.6: Left: plan of the Pierre Auger Observatory. Each dot represents a surface detector station and the lines represents the limits of the fluorescence detectors field of view. Right: detected hybrid event with color coded information about the arrival time. The size of the surface detector station codes the signal force. Both taken from [13].

the fluorescence detector can only be used in clear moonless nights. Thus, the duty cycle is approximately 13% [11].

An example of a hybrid event can be seen in figure 2.6, whereas hybrid means, the shower is detected by the surface detector as well as by the fluorescence detectors. The great benefit of hybrid events is the possibility of the observation of cosmic rays by complementary techniques and thus combining the excellent energy resolution of the fluorescence detector and the large duty cycle of the surface detector [11].

FAMOUS

The method of choice for observing low light level fluorescence showers has been photomultiplier tubes for years. A promising technique as a possible replacement of photomultiplier tubes are silicon photomultipliers (SiPMs), also referred to as Geiger-mode avalanche photodiodes (G-APDs). At III. Physikalisches Institut A, RWTH Aachen University, a SiPM-based telescope has been developed which is known as FAMOUS. The acronym stands for „**F**irst **A**uger **M**ulti-pixel photon counter camera for the **O**bservation of **U**ltra-high-energy air **S**howers“. A seven pixel version of the telescope has already been build. This will be upgraded to a 64 pixel version soon. In this chapter the basic concepts for understanding SiPMs are introduced. This is followed by the presentation of the FAMOUS baseline design and its data acquisition system.

3.1 Silicon photomultipliers

SiPMs in general are based on junctions of p- and n-doped semiconductors referred to as photodiodes [15]. At the area of transition between both contrary doped regions, electrons and holes recombine, thus a depletion zone develops. This can be broadened by applying a reverse bias voltage V_{bias} . A schematic sketch can be found in figure 3.1. Due to the depletion, a high voltage electric field is formed. If a photon passes the depletion zone, it may be absorbed and an electron hole pair is created according to the photoelectric effect. Both, electron and hole, are drawn out of the depletion zone by the electric field. When reaching an adequate energy by the acceleration process, they can themselves create new electrons and hole pairs by impact ionization. If a sufficiently large bias voltage is supplied, the photodiode works in Geiger mode. This means the charge, which can be measured outside the depletion zone, is equal for each photon passing the sensitive area and causing a cell breakdown. The breakdown voltage V_{break} is the minimum voltage that has to be applied for a photodiode working in Geiger-mode. The difference between bias and breakdown voltage is referred to as over voltage V_{ov} :

$$V_{\text{ov}} = V_{\text{bias}} - V_{\text{break}} . \quad (3.1)$$

To stop the avalanche of produced carriers of charge, a quenching resistor is connected in series with the G-APD. The avalanche of charge originated by a passing photon leads to a rising voltage at the quenching resistor. Thus, the voltage at the G-APD decreases down to the breakdown voltage. This prevents another emergence of avalanche and the system returns to the initial state. During the process of recovery, additional breakdowns can occur, which results in a lower signal level. Multiple G-APDs or cells connected in parallel are named SiPM.

As a result of the Geiger mode, each cell on a SiPM can only detect one photon at once, if it is absorbed. The produced signal is approximately the same for each cell

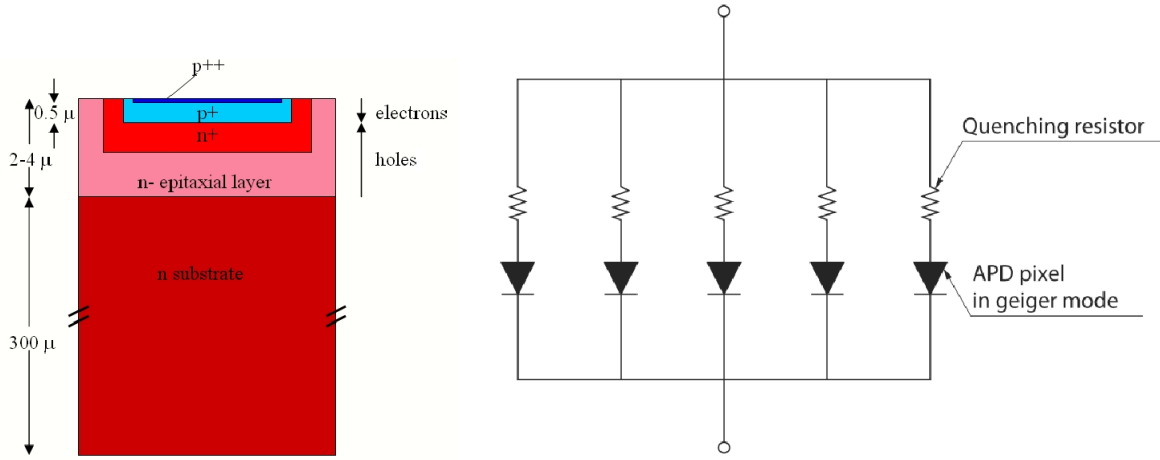


Figure 3.1: Left: schematic sketch of an avalanche photodiode. Taken from [16]. Right: equivalent circuit diagram of a SiPM array. Taken from [17].

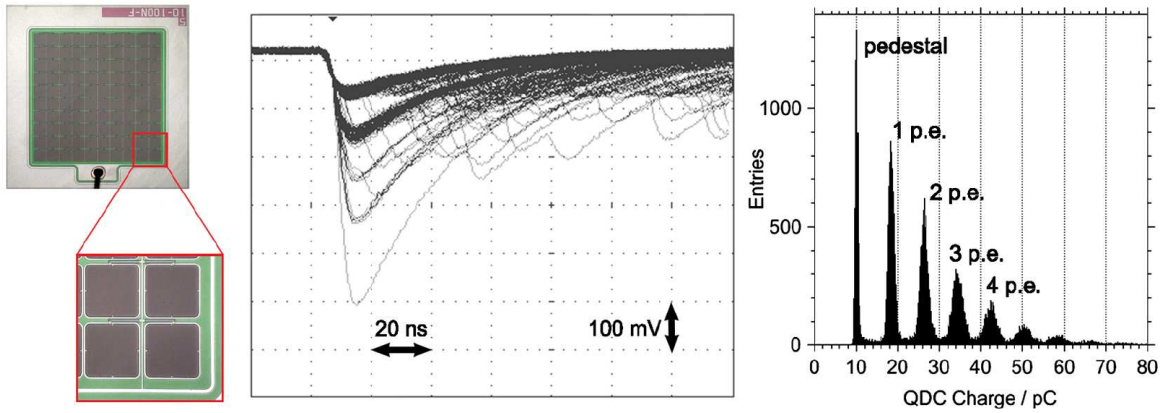


Figure 3.2: Left: photograph of a SiPM and a zoom to four cells. Center: Oscilloscope screenshot of the signals of a SiPM the number of cell breakdowns is clearly distinguishable. Right: charge spectrum measured for a SiPM, who is illuminated by a pulsed LED. The photon equivalent (p.e.) is the charge caused by a photon. Taken from [18].

breakdown. With the help of a SiPM cell array, the counting of photons becomes possible, as multiple cells can break down in a short time span. In figure 3.2, the distinction between the different numbers of cell breakdowns is clearly visible.

The photodetection efficiency (PDE) can be calculated by [15]:

$$\text{PDE}(\lambda) = \text{QE}(\lambda) \cdot f_{\text{geom}} \cdot P_{\text{break}} \quad (3.2)$$

Here, QE describes the quantum efficiency, therefore the probability, if a photon passing the sensitive area is absorbed and creates an electron-hole-pair. The geometric fill factor f_{geom} is the ratio of sensitive area to the total area of the detector. It is less than one due to the implementation of the quenching resistor and the connections of the cells of each SiPM. The breakdown probability P_{break} gives the chance for a created electron hole pair to start an avalanche and to cause the breakdown. Using a sufficiently high

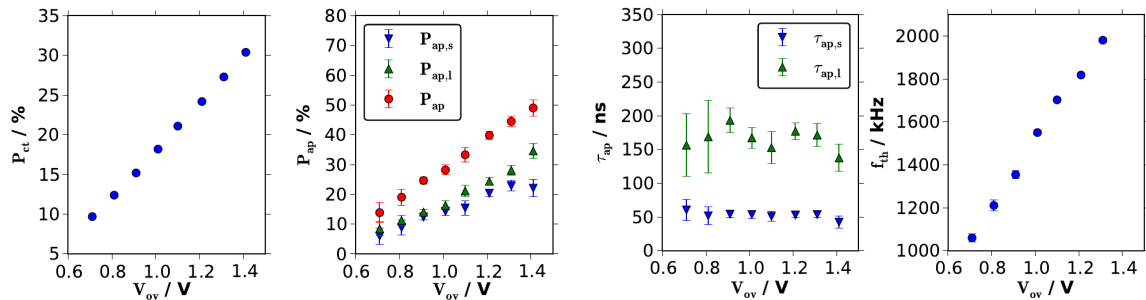


Figure 3.3: The dependency of the over voltage for the probability of the different noise phenomena. P_{ct} refers to optical crosstalk and P_{ap} to after pulsing probability. The frequency of the thermal noise is described by f_{th} . In case of the after pulsing, two different time constants τ_{ap} are observable. Taken from [22].

over-voltage, P_{break} is close to 100%. The PDE depends on the photon wavelength λ [15].

In the UV region, a PDE of approximately 35% can be achieved with the SiPMs used for FAMOUS [19].

Not only the undetected photons have to be studied, but also the dark rate, since also without any light reaching the SiPM, a signal can be measured. This is produced by noise phenomena, namely thermal noise, optical crosstalk and after-pulsing. These are discussed in the following paragraphs.

Thermal noise: Instead of photons, an electron hole pair can also be created by thermal excitation. The resulting signal through the breakdown can not be distinguished from a signal initialized by a photon. This effect is studied in [20].

Optical crosstalk: During the avalanche of the breakdown, the creation of a photon by recombination of an electron and a hole is possible. The photon can enter a neighboring cell and initialize a breakdown of this cell. This effect has been studied in [21].

After-Pulsing: During the breakdown of a cell, individual electrons can be captured by defects in the silicon lattice. Due to a delayed release after the recovery of the cell, a new breakdown can be initialized. In [21], after-pulsing is studied in much more detail. As seen in figure 3.3, it exist two different time constants for the after-pulsing.

The probability for the different noise phenomena is a function of the over voltage, which becomes is presented in figure 3.3.

The different noise phenomena are not independent of each other. A breakdown due to thermal noise can be accompanied by optical crosstalk and followed by an after-pulse. To summarize these effects, the dark count rate can be studied. For a given SiPM, this rate depends only on environment conditions. The new generation of SiPMs manufactured by Hamamatsu promises a significant lower after pulsing rate and with the use of trenches, the after pulsing probability can lowered [23].

Beside the noise characteristics, the over voltage determines all important properties of the SiPM, for example the gain. Thus, during a measurement, the over voltage and the gain have to be kept constant. In order to achieve this, the temperature dependency

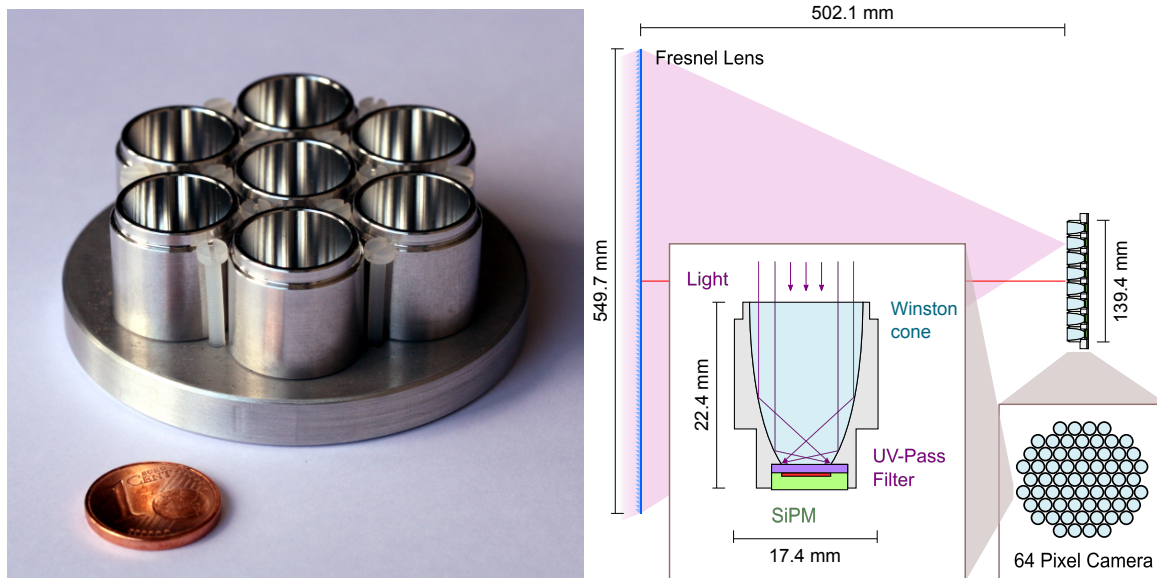


Figure 3.4: Left: Focal Plane of the FAMOUS telescope prototype, taken from [24]. Right: Schematic sketch of a pixel consisting out of Winston cone, UV-pass-filter and SiPM, taken from [22]

of the breakdown voltage is important. The relation between temperature and V_{break} is linear in good approximation[21]:

$$V_{\text{break}}(T) = V_{\text{break}}(T=25^{\circ}\text{C}) + \beta \cdot (T - 25^{\circ}\text{C}) . \quad (3.3)$$

The progression coefficient β is 56 mV/K for the used SiPMs [19]. Hence, if the development of the temperature is known, the over voltage can be fixed to a specific value.

3.2 The telescope prototype FAMOUS

To study the possibility of air shower detection using SiPMs, the FAMOUS prototype has been developed by the III. Physikalisches Institut A, RWTH Aachen University. In this section, the basic construction, as well as the data acquisition system and the slow control are presented.

3.2.1 The baseline design

The FAMOUS prototype has a relatively simple refractive design [22]. The main components are a Fresnel lens and a focal plane consisting currently of seven pixels arranged in a hexagonal grid. In this context, a pixel is the combination of a Winston cone and a SiPM. In figure 3.4, a schematic sketch of a pixel can be found as well as a photograph of the focal plane of the current version of the prototype. In the figure, the focal plane and the outline for the 64 pixel version is presented as well.

In the refractive design, the Fresnel lens is the focusing component. With a diameter of $d = 549.7$ mm, it has a focal length of 502.1 mm and 10 grooves per millimeter [22].

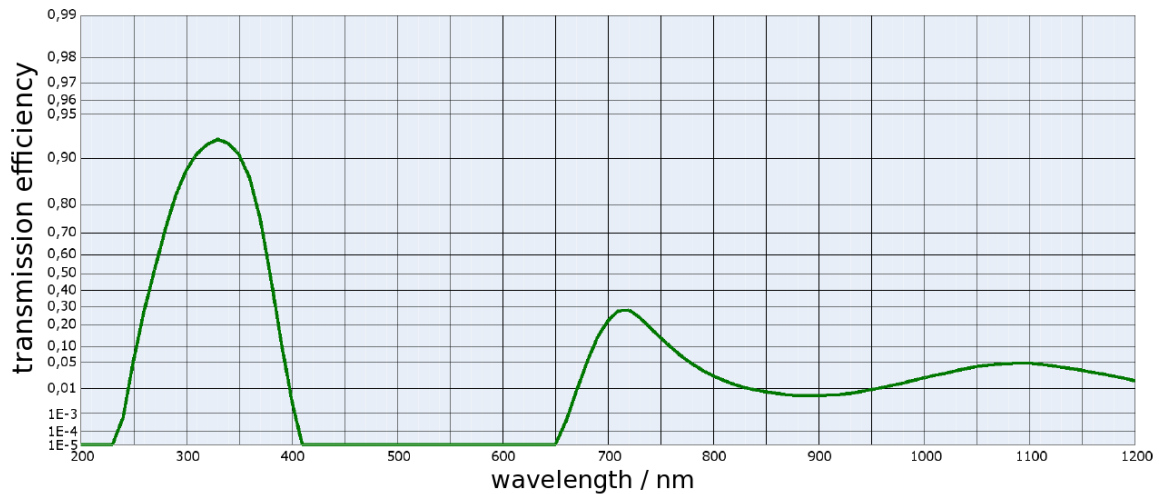


Figure 3.5: Transmission efficiency of the Schott UG-11 UV-pass filter. The main transmission is in the UV regime, which is the wavelength area of the fluorescence light emitted by extensive air showers. Adapted from [29].

It is manufactured out of UV-transparent acrylic, thus the transmission efficiency is approximately 70 % [25]. As verified by experiments and simulations in [26], the optical properties of the lens are sufficient for the FAMOUS telescope.

The Winston cones are used as non-imaging parabolic concentrators [27]. Consisting of polished aluminum, they are manufactured in the III. Physikalisches Institut A, RWTH Aachen University. The entrance radius is 6.71 mm and the exit radius is 3 mm². In [28] the independence of the reflection power of the aluminum for different states of oxidation could be evidenced for the UV range.

With help of these cones, the light is led onto the SiPMs. The used SiPMs are Hamamatsu S10985-100C multi-pixel-photo counters [22]. More precisely, it is an array out of four single 3×3 mm² SiPMs (Hamamatsu S10362-33-100C). Hence, the totally covered area is 6×6 mm² which covers the whole exit aperture of the Winston cone.

The collected light is falling through a UV-pass filter, namely Schott UG-11 onto the SiPM [22]. As the main component of the fluorescence light is in the UV regime, the use of the filter enables an improved signal to noise ratio (c.f. figure 2.3 and 3.5).

In figure 3.6 the FAMOUS prototype can be seen together with its connected electronics. It contains the power supply and the data acquisition system. The latter will be discussed in more detail during the next section. The power supply is manufactured in III. Physikalisches Institut B, RWTH Aachen University. It supplies individual bias voltages for each pixel. Furthermore, the bias voltage is automatically adjusted for the temperature dependent breakdown voltage (c.f. section 3.3). Additionally, the temperature of each pixel is measured by the power supply. As a result of this ability, the power supply is referred to as FT-PC, which stands for „Fiber Tracker Power Control“.

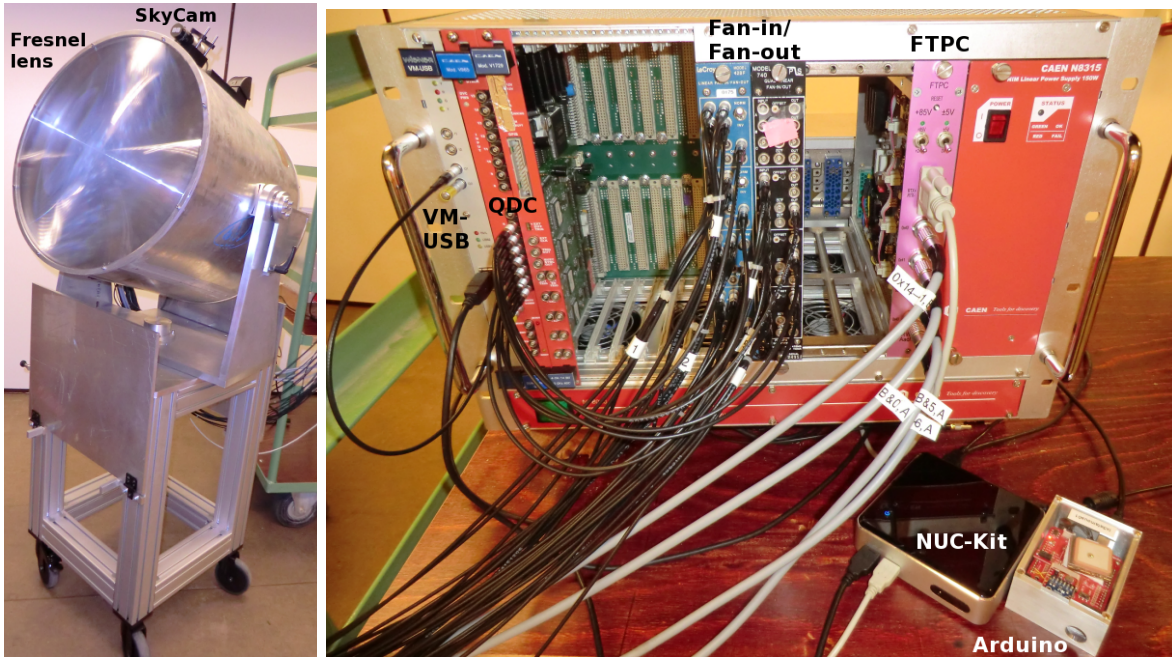


Figure 3.6: Left: image of the FAMOUS telescope. On top of the telescope, the SkyCam is mounted (c.f. chapter 4). Right: electronics of the telescope.

3.2.2 The data acquisition system

As a result of each pixel consisting out of four individual SiPMs, the first step is to calculate the sum of the four signals. Therefore, a fan-in/fan-out is used. Namely the LeCroy 428F for pixel 0 to 3 and PZS 740 for pixel 4 to 6. The next step is the charge to digital converter (QDC) CAEN V965 [30]. The sum-signal is converted to a digital output whereas two different output signals are handed out, which differ in high or low gain. This method achieved a good way of handling with high signals and also a good resolution. Via a Wiener VM-USB interface the QDC can be read out by a PC. All components of the read-out electronics are housed in a combined NIM-VME-Combi-Crate. The FTPC and the VM-USB interface [31] are connected to an Intel NUC-Kit, Model D54250WYK [32] hosting the DAQ software, a webserver and the database.

For interpretation of the recorded data, the understanding of the operation principle of QDC is essential. To convert the SiPM spectrum to a digital value, the voltage profile is integrated over 200 ns. The result is assigned to one of 4096 QDC channels. For one measurement, 10000 values are recorded with a frequency of 50 kHz, if not otherwise stated.

By the use of an Arduino Microcontroller and several environment sensors [33] the environmental conditions are monitored. Hereby the GPS position, the humidity, pressure, temperature of the environment as well as ambient light are recorded. In a later analyze, these variables can be tested, if they influenced the performance of the electrics or the data acquisition system.

The database is based on MySQL. It contains the environmental information as well as the information about the system, like bias voltage logs, runs and shifters, and the

calibration files. Also the recorded data are saved this way. A graphical presentation of the saved values can be found in the slow control interface, which is described in the next section.

3.2.3 The slow control interface

Via the slow control interface the FAMOUS telescope can be controlled and the data taking monitored. In figure 3.7, a screenshot of the „dashboard“ can be found.

On the one hand, the interface enables the monitoring of the environmental conditions, which are presented in several plots. The system can be monitored as well, concerning the over voltage, progression coefficient and temperature of the pixels as well as the state of the system itself. On the other hand, the system enables to create new runs, start calibration routines, set an over voltage and start the data taking. As well it reports the status of the components which are connected, like FTPC, QDC, environment sensors and the SkyCam. The latter will be introduced in the next chapter.

The taken data are visualized with use of the arithmetic mean value of each measurement abbreviated by q_{mean} . The development of q_{mean} is displayed (c.f. tab events on [1]), as well as two consecutive measurements are used to illustrate the development during the run (c.f. figure 3.7).

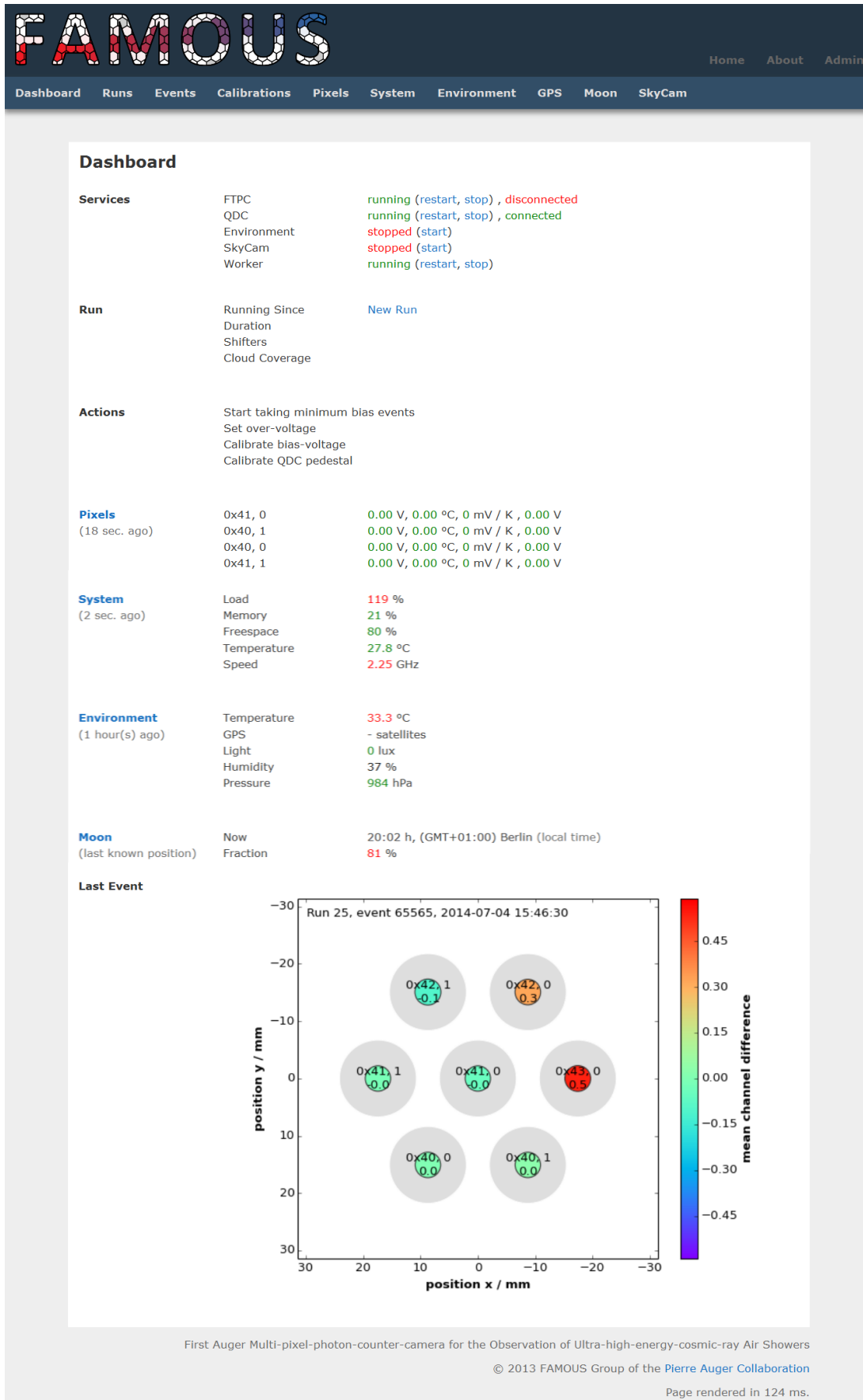


Figure 3.7: Screenshot of the „dashboard“ of the slow control interface. Taken from [1].

The SkyCam night sky camera

The night sky permanently changes during a night. Not only stars or planets move through the field of view of a telescope, the cloud coverage may vary as well. Knowledge on these conditions is essential for astronomical observations and for fluorescence and Cherenkov measurements. For this purpose the SkyCam module has been developed for the FAMOUS telescope during this work.

The SkyCam is based on a CMOS camera (Complementary Metal-Oxide-Semiconductor) combined with a compact fixed focal length lens of $f = 8.5$ mm. The used components are the ALccd-QHY 5L-II camera by Astrolumina [34] and the 58-000 lens by Edmund Optics [35].

The SkyCam has a resolution of 1280×960 pixels, each with the dimensions of $3.75 \times 3.75 \mu\text{m}$ [34]. The whole detector plane covers 4.83×3.63 mm. Exposure times can range from $20 \mu\text{s}$ to 99 s. The gain can be selected within the range of 1 to 1000.

In a first step, the image distortion of the captured images is corrected using the OpenCV software package, which is presented in detail in the next section. When used together with the FAMOUS telescope, the SkyCam enables the detection of visible stars with the help of the Astrometry.net software. This method is introduced in section 4.2.

4.1 Correction of the image distortion

In photography multiple kinds of aberration occur. The OpenCV library provides packages for the correction of this distortion [36]. A brief introduction to this topic is followed by the characterization of the used setup and the measurements as well as their results.

4.1.1 General approach

The distortion of an image can be described by two components: the tangential and the radial distortion [36]. The radial component leads to the „fish-eye effect“ or barrel distortion. And the tangential distortion is caused by a non vertical incidence of light on the optical system. For the correction, the determination of five distortion coefficients, k_i and p_i , is necessary.

The radial component of the correction is described by:

$$x_{\text{corrected}} = x(1 + k_1 r^2 + k_2 r^4 + k_3 r^6) \quad (4.1)$$

$$y_{\text{corrected}} = y(1 + k_1 r^2 + k_2 r^4 + k_3 r^6) \quad (4.2)$$

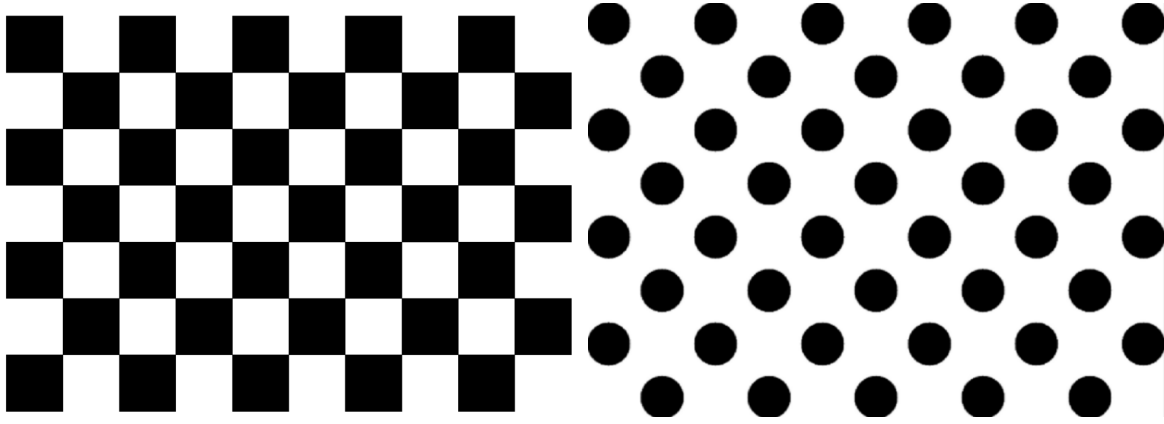


Figure 4.1: Used patterns for the SkyCam calibration. Left: chessboard pattern. Right: asymmetrical circles pattern. Taken from [36].

The tangential distortion can be corrected by:

$$x_{\text{corrected}} = x + [2p_1xy + p_2(r^2 + 2x^2)] \quad (4.3)$$

$$y_{\text{corrected}} = y + [p_1(r^2 + 2y^2) + 2p_2xy] . \quad (4.4)$$

In these formulas, x and y are the position of an image point in Cartesian coordinates, whereas the origin is set to the image center. The distance from the origin to a point is given by r . For these values, the following unit conversion is used:

$$\begin{pmatrix} x \\ y \\ z \end{pmatrix} = \begin{pmatrix} f_x & 0 & c_x \\ 0 & f_y & c_y \\ 0 & 0 & 1 \end{pmatrix} \begin{pmatrix} X \\ Y \\ Z \end{pmatrix} . \quad (4.5)$$

Here, f_x and f_y are camera focal length and the optical center is expressed by (c_x, c_y) , which are given like X and Y in pixel coordinate. The matrix in equation 4.5 is referred to as camera matrix.

To determine the distortion coefficients k_i and p_i , the photograph of a reference pattern can be used. Among others, two patterns are supported by the OpenCV library and used in this work: a chessboard-like pattern and a asymmetrical circles pattern. Both can be seen in figure 4.1.

The used algorithm detects certain marks in the pattern, referred to as image points \vec{P}_{image}^i . In case of the chessboard, the inner corners are used, whereas in case of the circles grid, the center of the circles itself are used. The detected coordinates are compared to the saved values about the pattern marks, referred to as object points $\vec{P}_{\text{object}}^j$. With use of the formulas 4.1 to 4.4, the distortion coefficients are calculated. For a detailed description c.f. [36].

In the following measurements, the robustness of the algorithm is tested by using the average re-projection error, abbreviated as ϵ as a characteristic variable.

$$\epsilon = \frac{1}{s} \left(\frac{1}{n} \sum_{i=1}^n \left[\frac{1}{m} \sum_{j=1}^m |T(\vec{P}_{\text{object}}^j) - \vec{P}_{\text{image}}^i| \right] \right) . \quad (4.6)$$

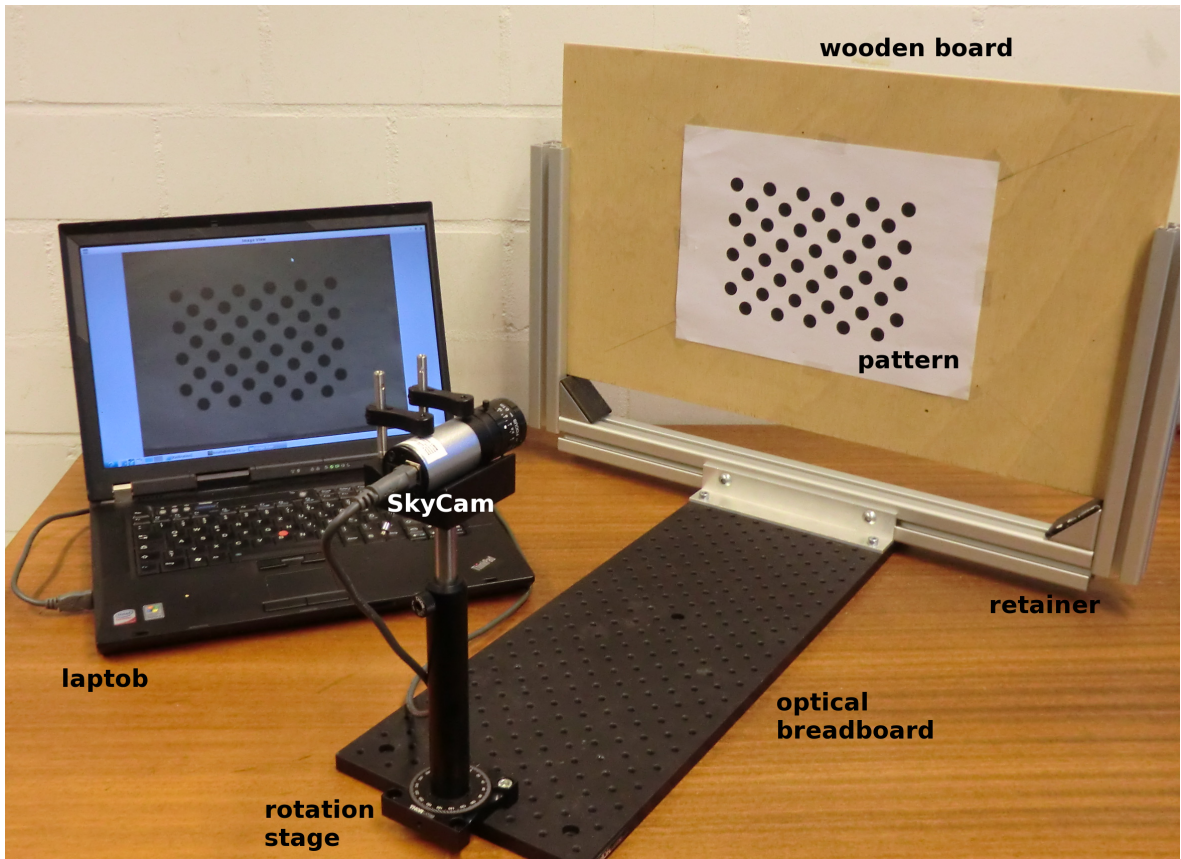


Figure 4.2: Setup used for the calibration of the SkyCam.

For each of the n images taken into the calibration, a re-projection error is calculated. It stands for the absolute norm between the transformation of the object points and the image points per number of image points m . The average re-projection error ϵ is calculated by the average mean of the re-projection errors of the individual images. For better comparability of the two patterns, ϵ divided by the object points spacing s , given in the same unit conversion, and gives as percentage. The transformation T is the projection of 3D points to an image plane. It is realized by a matrix multiplication with the camera matrix and a projection matrix, which depends on the distortion coefficients. For more details c.f. [37].

4.1.2 Experimental setup

The setup used for the calibration of the SkyCam can be seen in figure 4.2. Upon the one side of an optical breadboard, the SkyCam is mounted on a rotation stage. On the other side of the board, a retainer is attached. This contains a wooden board, on which in turn the pattern can be attached. The optical breadboard and the rotation stage are produced by ThorLabs. The distance between the SkyCam and the pattern is approximately 50 cm, which is sufficiently large enough for the producing of sharp images with $f = \infty$. The pattern is fixed in the center of the board and the SkyCam is directed to the center of the pattern.

Since the purpose of the SkyCam is to observe the night sky, the focus is locked to its

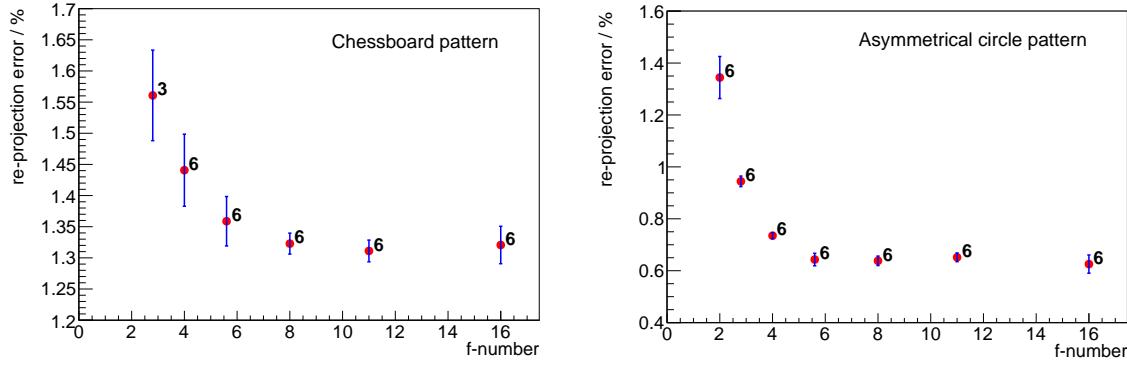


Figure 4.3: Measurements for the chessboard pattern (left) and the asymmetrical circle pattern (right), performed in color mode. The reading is performed sixfold with stable environmental conditions (ambient light, temperature). The number at the data point symbolizes the measurements with successful calibration.

maximum, referred to as infinity by the datasheet [35]. The focal ratio, also referred to as f-number remains variable. This quantity is the ratio of focal length and the diameter of the entrance pupil [38]. If this ratio variates by the factor of $\sqrt{2}$, the light intensity halves.

Several series of measurements have been performed, all based on the same principle. To gain one re-projection error measurement, ten pictures are taken under constant ambient light and temperature. Based on these images, the calibration procedure is performed. The focal ratio is varied, following the standard full-stop f-number scale from 1.4 to 16. This scale marks the points at which the light intensity halves for a constant exposure [38]. During the measurement the exposure time is adjusted to the f-number and is 320 ms for a focal ratio of 16, and the gain is fixed at 50. Unless otherwise stated, the SkyCam is aligned perpendicular to the pattern, referred to as an angle of 0° .

Within several series of measurements, the robustness of the method is studied as well as the angular dependency. Since the SkyCam can be operated in monochrome and in color mode, the influence of this parameter is investigated as well.

4.1.3 Results

As the result of the calibration is used hereafter, the values have to be reliable. For this purpose, the uncertainty is studied by performing the measurement six times for each focal ratio. To evaluate this measurement, the mean $\bar{\epsilon}$ and estimator for the standard deviation are calculated [39]:

$$\bar{\epsilon} = \frac{1}{N} \sum_i \epsilon_i \quad (4.7)$$

$$\tilde{\sigma}_\epsilon^2 = \frac{1}{N-1} \sum_i (\epsilon_i - \bar{\epsilon})^2 . \quad (4.8)$$

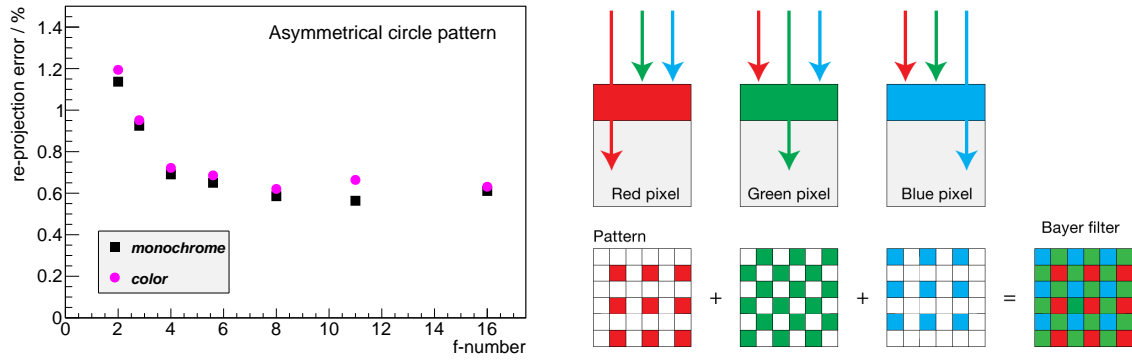


Figure 4.4: Left: comparison of mono and color mode of the SkyCam. The measurement is performed with the asymmetrical circle pattern. Right: illustration of a Bayer filter mosaic. This filter system enables the color mode of the CMOS sensor. Taken from [26]

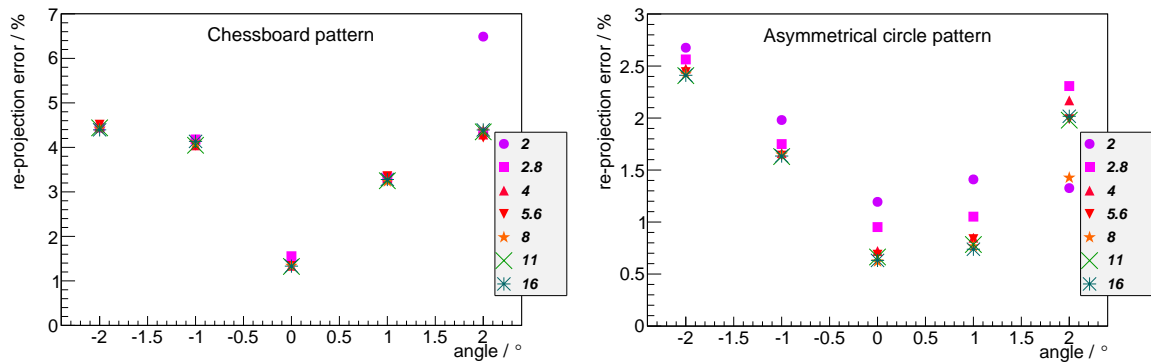


Figure 4.5: Measurement of the angular dependency of the re-projection error for the chessboard pattern (left) and the asymmetrical circle pattern (right).

The results of the measurements are presented in figure 4.3. For a small f-number some measurements do not lead to a successful calibration. This effect is more pronounced on case of the chessboard pattern. Here, measurements with a focal ratio up to 2.8 are affected, whereas for the asymmetrical circle grid, only the focal ratio of 1.4 could not be successfully completed. In both measurements, the re-projection error rises for smaller f-numbers. This could be caused by a loss of sharpness of the captured image. In both cases, the best performance is achieved for medial f-numbers.

In a next step, it is studied, if the mode of image taking, monochrome or color, has an influence on the calibration. To enable the the capturing of color images with a CMOS sensor, a Bayer filter mosaic is used [40]. Thus, red green and blue pixels are arranged in an array as seen in figure 4.4.

For the asymmetrical circle pattern, the result is presented in figure 4.4. The measurement performed with the asymmetrical circle pattern shows no significant difference in the behavior of the calibration. Although, the re-projection error is a bit larger for measurements in the color mode, which could be an effect of the interpolation with

help of the Bayer mosaic.

When performing the measurement with the chessboard pattern, the calibration could not be performed, irrespective of the focal ratio. This could be an effect of the different type of reference marks. In case of the asymmetrical circles pattern it is the center of a circle, whereas for the chessboard pattern, the corners of the squares are used. Hence a smearing of the margins of the pattern objects due to the Bayer filter could affect to the chessboard method.

Furthermore, the angular dependency of the performance of the calibration is studied. To do this, the angle of the orientation of the SkyCam towards the pattern is set with help of the rotation stage. At this, an angular scale in steps of one degree is printed. The angle is varied from -2° to $+2^\circ$, which is the maximum range, in which the pattern is totally visible in the taken image. For each angle and each focal ratio, one measurement is performed. The result of the measurements is presented in figure 4.5. As expected, the re-projection error rises when the angle increases. During this series of measurements, the calibration could not be successfully performed for all focal ratios, as well as in the former series. The behavior of the re-projection error is not symmetric around 0° . The most probable reason for this is an imprecise adjustment of the angle at the rotatable stage.

For the final calibration, the chessboard pattern is used, since a complete coverage of the field of view can be achieved. The asymmetrical circle pattern can not be used, as the algorithm can not handle when circles are too close to the image corners. The final calibration results in a re-projection error of $\epsilon = 1.44\%$ performed at a focal ratio of 4.

4.2 Detection of visible stars

The benefit of the SkyCam while working together with FAMOUS, is the opportunity to detect the visible stars. For this purpose, the Astrometry.net software is used. This software is introduced in the next section followed by a description of the operation principle of the SkyCam, when it is used together with FAMOUS.

4.2.1 Astrometry

The Astrometry.net software is developed to perform fast geometric hashing for automated astrometry [41]. Up on the basis of index files based on the 2MASS catalog („Two Micron All Sky Survey“), the field of view as well as the visible luminaries are determined. In this index files, the relative position of nearby quadruples of stars are deposited. This quadruples are referred to as skymarks [42]. The position are given in an unit system defined by the most distant stars (c.f. figure 4.6). Hence the index files are not affected by scale, translation and rotation.

As the number of stars and other luminaries is enormous, there are multiple index files, which differ in the diameter of the contained quadruples. Whereas the index files for the large skymarks cover the whole sky, the index files for skymarks with smaller diameter are split up into 12 respectively 48 individual files.

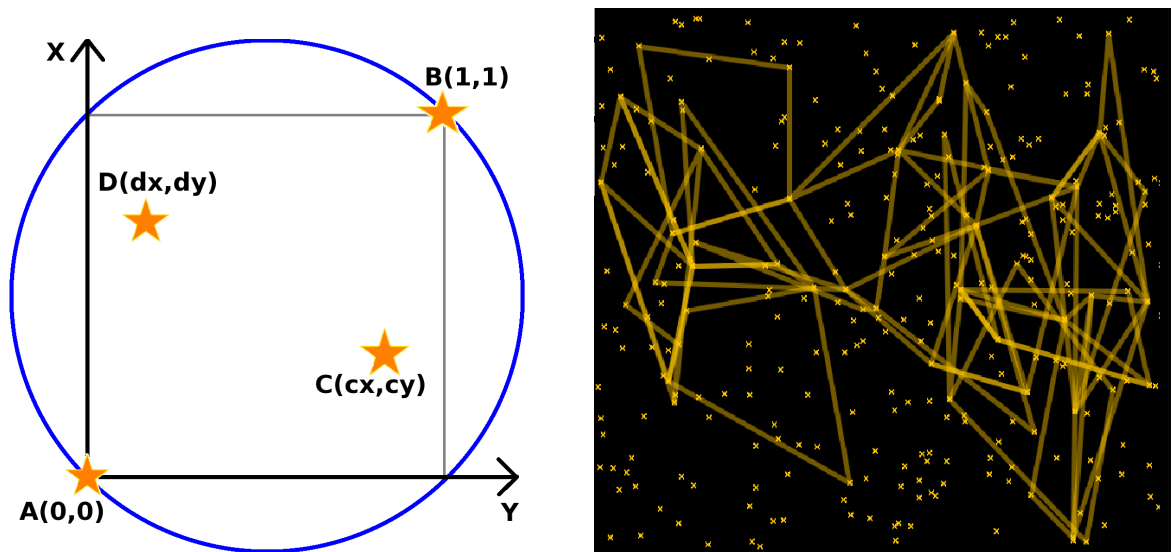


Figure 4.6: Left: Example of a quadruple for the illustration of the units used in the Astrometry.net index files. Right: Illustration of skymarks contained in an index file, taken from [42].

To analyze an image, several steps have to be computed. First of all, the light sources in the input image have to be detected and their pixel conditions are saved [41]. These positions are written to a WCS file, sorted by their brightness. The next step is to form quadruples out of these stars, starting with the brightest and calculating the corresponding skymark coordinates. These are compared to the skymarks in the index files. If a skymark is matching, there is a candidate for the position and the rotation of the field of view. If two quadruples confirm the same candidate, the candidate is stored as a match and the algorithm moves on. After looping over all skymarks in the investigated image, the list of matches is consulted to perform a further, a more detailed and more slower position verification. If this also succeeds, the image is marked as „solved“. For a more detailed discussion of the algorithm c.f. [42]. For a successfully „solved“ image, several output files are created. These contain the pixel positions and the positions in equatorial coordinates of the stars from the index which are in the field of view. In the output files, the pixel coordinates of the detected sources are stored as well. Also the description of the solution process, for example which index file was used to analyze the image is noted. The found coordinates for the center and the dimensions of the field of view are stored as well. To illustrate the detected sources as well as the stars from the index and the constellations in the field of view, plots are created.

The Astrometry.net package, can be used as a web based version as well as an offline version. When using the offline version, several variables could be specified to speed up the solving process. These are explained in the following section.

4.2.2 Operating principle

As seen in figure 3.6, the SkyCam is mounted on top of the FAMOUS telescope and is adjusted parallel to its optical axis.

During a single night or from night to night, the light conditions are much different from each other when e.g. the full moon is in the night sky or only a few stars are in the field of view due to clouds. To enable an autonomous use of the SkyCam an automatic adjustment of the exposure time is necessary. To perform this, the brightness measured for each pixel is put into a histogram, containing $n_{\text{bin}} = 256$ bins. This is done separately for each color in the Bayer filter mosaic, red, green and blue. For each color, the mean of the channel weighted by the number entries is calculated. In a final step, the mean of the results for the three histograms is calculated (c.f. 4.8). This mean, referred to as b_{measured} , is compared to a desired value b_{norm} . Whereas b_{norm} is 30, but can be set by the user. To reach the desired brightness, the exposure time t_{exp} is adjusted by multiplication with $b_{\text{measured}}/n_{\text{bin}}+1$, if b_{measured} is greater than b_{norm} . If the ratio is vice versa, the exposure time is divided by this factor. This enables a fast adjustment of the desired exposure time. Whereas the exposure time is only adjusted, if the difference between b_{measured} and b_{norm} is greater than 5. This is done to avoid continuous variation for t_{exp} so the performance of the SkyCam is not affected by this change.

During a measurement with FAMOUS, the SkyCam takes continuous images without switching the CMOS chip on and off to avoid unwanted side effects. Images in an adjustable distance of time are corrected by the algorithm described in section 4.1. For this corrected image the Astrometry.net algorithm is started. Test measurements show the problem that due to long exposure times, several hot pixels occur (c.f. figures 4.7, 4.8). In order to do not affect the algorithm, a downsampling by the factor of four is applied on the image. This enables the algorithm to ignore the hot pixels and still detect the stars, since they cover more than one pixel. Thus the field of view of the SkyCam is $30 \times 24^\circ$, only the index files with a skymark diameter greater than 30 arcminutes are used. All in all twelve index files are provided, which differ in the diameter of the contained skymarks. These files cover the whole sky, so no more specification is needed.

Furthermore, to speed up the process of solving, maximal 60 sources are consulted to the algorithm, whereas first the brightest 20 are used and then the sources from [21, 40], [41,50] and [51,60] are used. For each range of provided stars, all provided index files are run through. During the test measurements, most images which could be successfully solved are solved in the first three runs. To avoid an overload of the DAQ system, the processing-time-limit for each run is set to 30 s, but is rarely used.

Figure 4.7 can be used as an example for a successful solving process. Next to the input image, an image created by Astrometry.net. This includes an annotation plot, which names the stars in the field of view. The other information, like the center of the field of view and its orientation are stored in a WCS file, which can be read out via a provided program „wcsinfo“.

The images which are taken by the SkyCam or produced by Astrometry.net are available in the slow control interface in the section SkyCam.

Commissioning of FAMOUS

For the commissioning of the telescope, several steps have to be performed. The breakdown voltage of the SiPMs has to be determined, since most of the properties of the SiPMs depend to accurately determine and control of the over voltage. Several methods are presented for the determination of the breakdown voltage. One classical approach is based on the „finger spectrum“ of dark noise. Another does not rely on the measurement of dark noise but on the gradient in the QDC signal when the bias voltage reaches the breakdown voltage. With help of the breakdown voltage, the overvoltage can be determined (c.f. 3.1). Furthermore, the pedestal of the SiPMs signal due to the QDC has to be calibrated. Beside the electrical components, also the optics have to be adjusted, so that the Fresnel lens is focusing best on the SiPM camera.

5.1 Determination of the break down voltage of SiPMs

The power supply via the FTFC enables to set an individual bias voltage for each pixel. However as each pixel is a combination out of four SiPMs, the breakdown voltage differs due to component tolerances. In this section, multiple methods are presented for the calibration of the breakdown voltage. First, two methods based on the finger like QDC spectrum are introduced. These can be used to determine the breakdown voltage as well as the gain of the SiPMs. Secondly, a method based up on the increase of the QDC mean value for voltages beyond the breakdown voltage is presented.

The SiPMs are manufactured by Hamamatsu and each SiPM is delivered with a data sheet, on which the recommended bias voltage is noted, abbreviated by V_H . This voltage equals approximately one volt over voltage. As the power supply can be only supplied for a complete pixel, i.e. an array of four SiPMs, the individual bias voltages are averaged (c.f. table 5.1).

5.1.1 Finger spectrum method

The basis of this method are the distinguishability of photo equivalents (c.f. figure 3.2).

The data acquisition system of FAMOUS is modified for this measurements. Instead of the former used commercial Fan-in/Fan-out, a custom made module is used, manufactured in the III. Physikalisches Institut A, RWTH Aachen. It provides a single calibration channel in addition to the summarized output, which is used in the following.

For a given voltage, one QDC measurement is performed in darkness and the resulting high gain histogram is stored for the further analysis. For one voltage, 1000 single

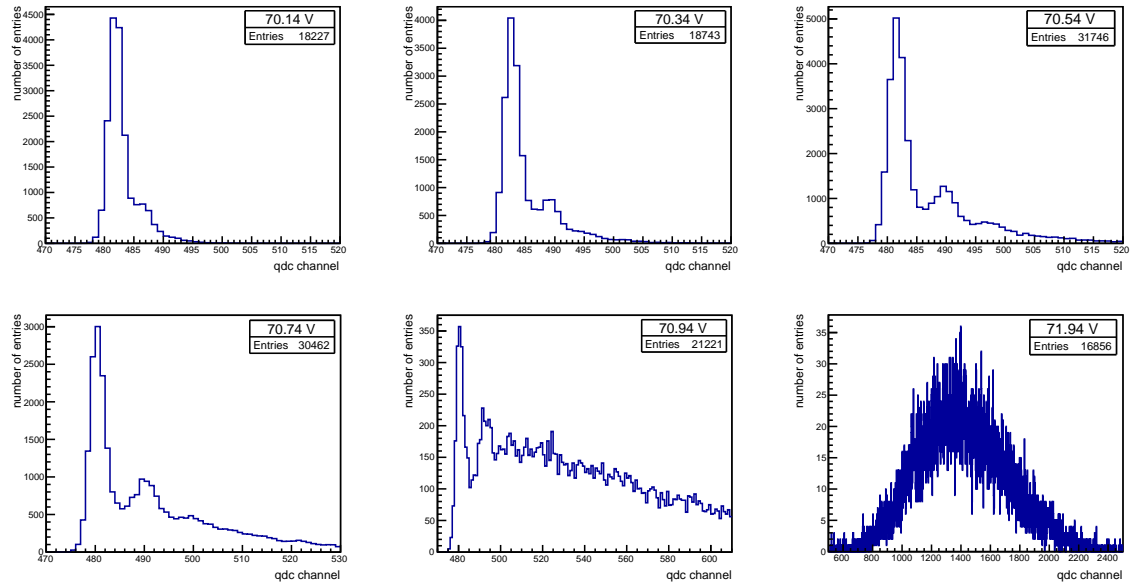


Figure 5.1: Finger like Spectrum as result of a QDC Measurement performed in darkness. The number of entries are plotted against the QDC channel. The bias voltage increases up right (70.14 V), down left (71.14 V) and belong to pixel 0, which V_H is 70.61 V. The distance between two peaks is proportional to the gain.

measurements are performed, whereas the number of QDC values per measurement variates. This process is carried out for voltages between $[V_H-1, V_H+1]$ separated by 0.2 V. For the later correction of the temperature dependency, the temperatures of the individual pixels are recorded as well and stored in the database.

The measurement results in QDC spectra, as they are presented in figure 5.1. For a part of these spectra, individual peaks are detectable. The spacing between the single peaks is proportional to the gain, thus there exist different methods for the determination. Two of them are presented in the following paragraphs.

Peak detection

The detection of the peaks can be performed with help of the data analysis framework ROOT. As a first step, candidates for the peak positions are detected via the TSpectrum class. Based upon this first estimation, the position of the minimum between two peaks is determined. Hence the borders for the domains of single peaks are known. To the upper third of a peak, a Gaussian function is fitted. As the detection of the first peaks works best, only the first two are used to determine ΔQ , which is proportional to the gain. The proportionality factor is $1/e$, with e represents the elementary charge. For the determination of the over voltage, the knowledge of ΔQ is sufficient.

Fourier transformation

Beside the detection of the peaks, a Fourier transformation can be used to determine the gain for a measured finger spectrum. First of all, the used histogram is normalized.

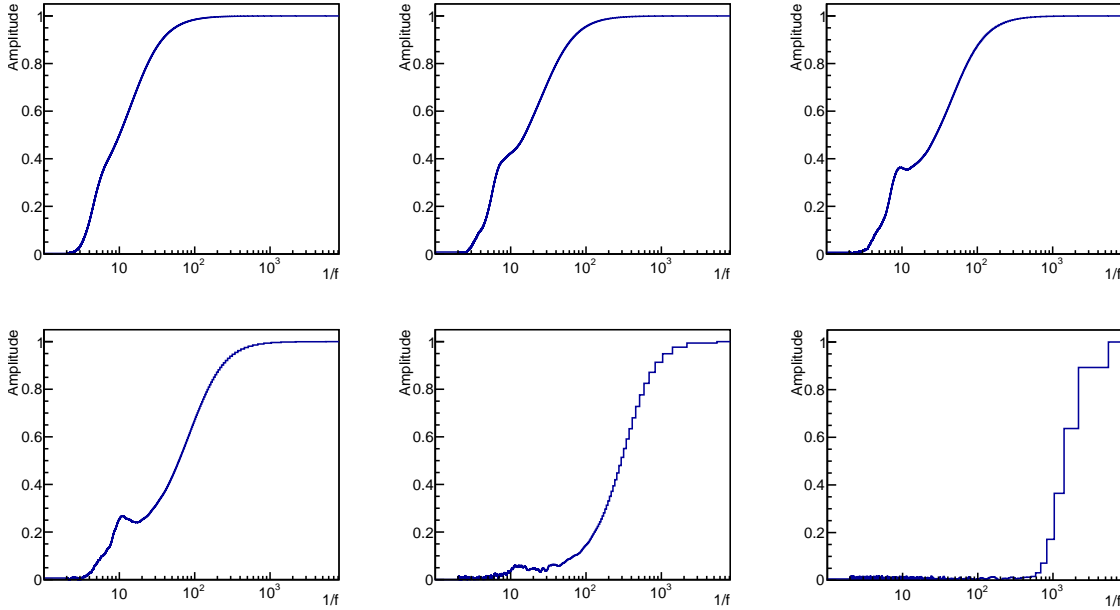


Figure 5.2: Fourier transformation for the QDC spectra in figure 5.1. The gain equals the position of the first peak. For better visibility, the x-axis is displayed with a logarithmic scale.

With help of the analysis framework ROOT a Fourier transformation is performed. Plotting the amplitude of the Fourier transformation coefficients against the inverse of the frequency leads to histograms as they can be seen in figure 5.2. Since the spacing between two fingers in the original finger spectrum is proportional to the gain, the gain is one of the main frequencies in the frequency spectrum. It equals the position of the first maximum from the right. To determine the exact position of this maximum, a Gaussian function is fitted to the peak, in the range where the amplitude is higher than the level in the minimum. To increase the robustness of this method, only maximums which differ more than 2% from their background are used.

Both methods result in the determination of the gain. The breakdown voltage equals the voltage where the gain or ΔQ is zero. Thus by plotting ΔQ against the voltage, the breakdown voltage corresponds with the x-axis intercept. This is determined by a linear regression.

To compensate the temperature dependency of the breakdown voltage, equation 3.3 is used. The results of these methods are summarized in table 5.1 in the next section.

It turned out, that the number of fingers in the spectra of a measurement performed in dark is not sufficient for the Fourier transformation method. Due to this, an additional setup has been developed. As a further improvement, this method enables the use of the summarized outputs.

To obtain the necessary finger spectra it is planned to use a pulsed UV-LED. This LED is connected to an optical fiber which conducts the light to an adapter in the backplane

of the FAMOUS telescope. Through reflection at the Fresnel lens, the pixels are illuminated. The LED is pulsed by the Universal Pulser, developed by III. Physikalisches Institut A, RWTH Aachen [43]. It enables an adjustment of the height and width of the voltage pulse, which is applied to the LED. The frequency of the pulses can be adjusted by an external trigger, for which a commercial function generator is used. The pulse width can be adjusted via a computer program, and its height via the control of the voltage by a power supply. An additional power supply is needed for the bias voltage for the pulser itself. With the help of an oscilloscope, the output pulse of the Universal Pulser can be monitored. Tests showed, that widths to a minimum of approximately 5 ns could be achieved. The pulse height can be adjusted from 5 V to 130 V. The maximum is due to the construction of the pulser.

This kind of light source is chosen to trigger multiple cells in one SiPM, within the trigger time of the SiPM. The pulse width is selected in such a way, that it is shorter than the recovery time of a single cell. The intensity of the resulting light pulse have to be sufficient low to achieve clearly visible fingers in the QDC spectrum. There are good prospects to benefit from this further developed method. Not only the Fourier transformation method can be proven in more detail, also the peak detection would benefit. With more clearly distinguishable peaks the determination of ΔQ is also improved. This can be realized by a linear regression when plotted the position of the maximum of the peak against the photon equivalent.

5.1.2 Gradient of the QDC signal

The measurement of a finger spectrum with well separated fingers can be a challenging task. In this section, an easier to carry out method is introduced.

This method is based on a simple measurement of the QDC mean in dependence of the bias voltage. No finger spectrum is needed, but also no information about the gain and the dark noise can be extracted.

In the range of $[V_H-7, V_H+1]$ around the recommended bias voltage V_H , the voltage is rasterized in steps of 0.01 V. For each voltage, and QDC measurement is performed and the QDC mean q_{mean} for the high gain histogram is stored. For a low statistical uncertainty, 10000 events are collected for the calculation of each q_{mean} . For all seven pixels, this measurement is performed simultaneously. An example measurement is presented in figure 5.3. Since the measurement is performed in a temperature controlled room, the temperature of the SiPMs during the measurement is sufficiently constant. After the completion of the measurement, the temperature of each pixel is read out and stored as well.

To determine the breakdown voltage, the voltage where q_{mean} starts to rise has to be calculated. To do this, the average out of the first N values is calculated as well as the associated standard derivation (c.f. equation 4.7 and 4.8). Hence the relative error σ_{rel} is calculated and its slope in each point. This quantity has an easily detectable knee, whereas the range of the slope is normalized to $[0,1]$. The knee is defined as the point where with decreasing voltage the $d\sigma_{\text{rel}}/dV$ does not continuously decrease any longer. For an error estimation, the strictness for the definition of a „continuously decrease“ is varied. An example result of this algorithm is presented in figure 5.4.

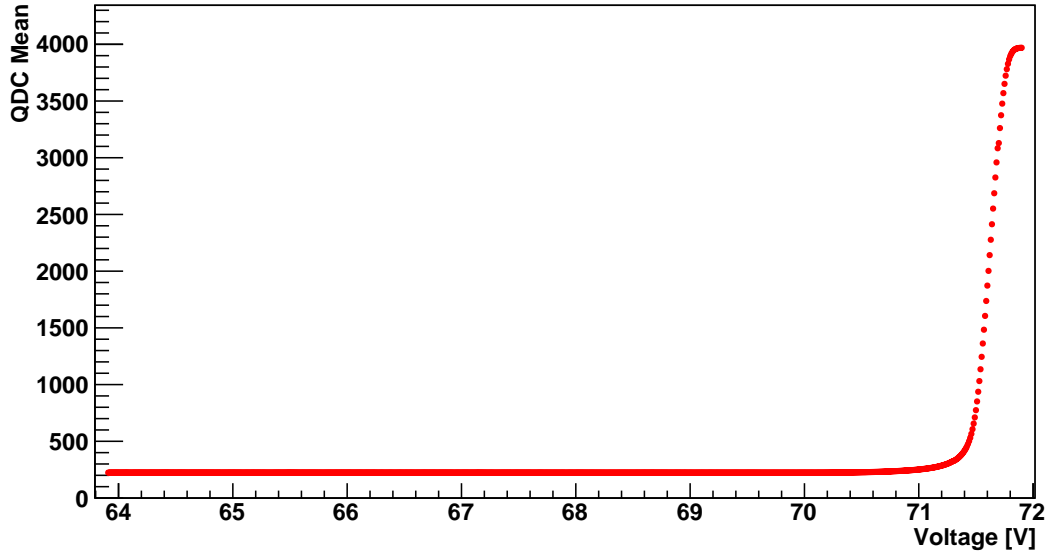


Figure 5.3: Example of a measurement for determining the breakdown voltage. The range of voltages is scanned in steps of 0.01 V. The measurement belongs to pixel number three.

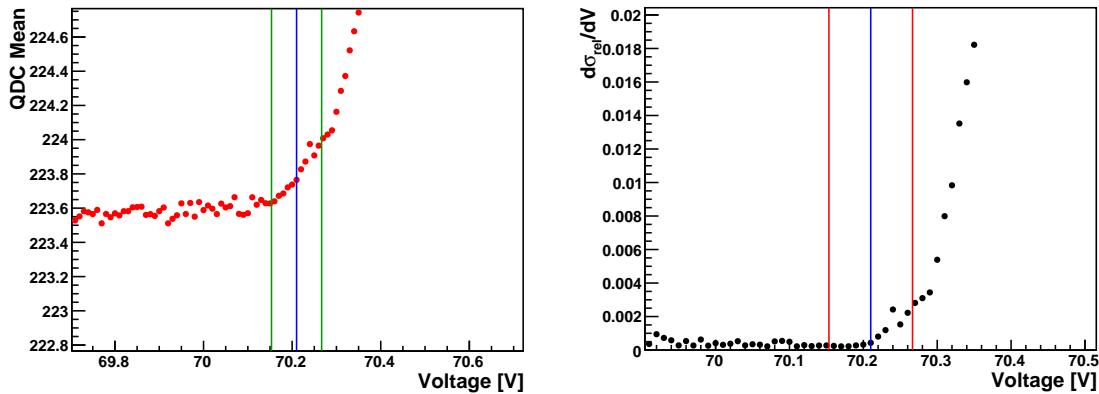


Figure 5.4: Example of a result for the evaluation of the gradient of the QDC signal. The measurement belongs to pixel number three. The centered line represents the calculate value, whereas the outer lines represent the one sigma region.

For the further use of these values, the voltages are corrected for their temperature dependence (c.f. 3.3) and given for the reference temperature of 25°. The results are summarized in the next section in table 5.1.

5.1.3 Result and comparison of the different methods

The determined breakdown voltages are summarized in table 5.1 together with the recommended voltage provided by Hamamatsu. It can be seen, that the values fit quite good among each other. The difference between the determined voltage and V_{textH}

| Pixel | $V_{\text{peak}} / \text{V}$ | $V_{\text{gradient}} / \text{V}$ | V_{H} / V | $V_{\text{H}} - V_{\text{peak}}$ | $V_{\text{H}} - V_{\text{gradient}}$ |
|-------|------------------------------|----------------------------------|---------------------------|----------------------------------|--------------------------------------|
| 0 | 69.44 ± 0.02 | 69.46 ± 0.05 | 70.61 ± 0.04 | 1.17 ± 0.04 | 1.15 ± 0.06 |
| 1 | 69.45 ± 0.03 | 69.38 ± 0.10 | 70.57 ± 0.04 | 1.12 ± 0.05 | 1.19 ± 0.11 |
| 2 | 69.55 ± 0.04 | 69.55 ± 0.10 | 70.73 ± 0.05 | 1.18 ± 0.06 | 1.18 ± 0.11 |
| 3 | 69.71 ± 0.04 | 69.72 ± 0.06 | 70.90 ± 0.04 | 1.19 ± 0.06 | 1.18 ± 0.07 |
| 4 | 70.32 ± 0.04 | 70.31 ± 0.04 | 71.41 ± 0.05 | 1.09 ± 0.06 | 1.10 ± 0.06 |
| 5 | 68.26 ± 0.02 | 70.48 ± 0.02 | 71.58 ± 0.07 | 3.32 ± 0.07 | 1.10 ± 0.07 |
| 6 | 69.89 ± 0.04 | 69.89 ± 0.01 | 70.97 ± 0.08 | 1.08 ± 0.09 | 1.08 ± 0.08 |

Table 5.1: Results for the determination of the breakdown voltage for the different methods. The values are valid for a temperature of 25 °C. V_{H} is the averaged recommended bias voltage by Hamamatsu. Here V_{peak} is determined as breakdown voltage with use of the finger spectrum and the peak detection method (c.f. 5.1.1). Whereas V_{gradient} is the result of the evaluation described in section 5.1.2. The calculated differences represents the over voltages which is included in V_{H} . The uncertainties result out of a Gaussian error propagation. For pixel number 5 the peak detection results in a too low value. This is due to a different breakdown voltage of the single SiPM of the array, which is used for this method. The other calculated over voltages are compatible to each other.

equals the recommended over voltage. The determined values are all compatible among each other in the one sigma ratio.

For pixel number 5, the result of the peak detection method is much to low. This could be due to different breakdown voltages of the single SiPMs of the array. since these method is based up only one of the four SiPMs of a pixel. The results of the fit for the determined peak positions and the linear regression for the determination of the breakdown voltage shows no abnormalities. The use of the pulsed LED as described at the end of the former section could improve this method, since all four SiPMs would be used.

5.2 Calibration of the QDC pedestal

Due to the data acquisition system, the QDC mean for a measurement without any signal is not zero, but at a certain pedestal. This pedestal is different for each pixel. For the further use of the recorded data, the individual pedestal can be subtracted. This improves the comparability of the individual signals of the pixels.

When the program for the calibration of the pedestal is started, all bias voltages are set to zero. After this is accomplished, a QDC measurement is performed and the average of the measurement q_{mean} is calculated. This value corresponds to the required quantity. To allow further measurements, the bias voltages are set to their initial values. The determined pedestals are stored in a calibration file, which is deposited in the database. The calibration can be invoked from the FAMOUS slow control website.

In figure 5.5, the benefit of the calibration becomes clearly visible. It shows a measurement performed in darkness with and without use of the pedestal calibration. The

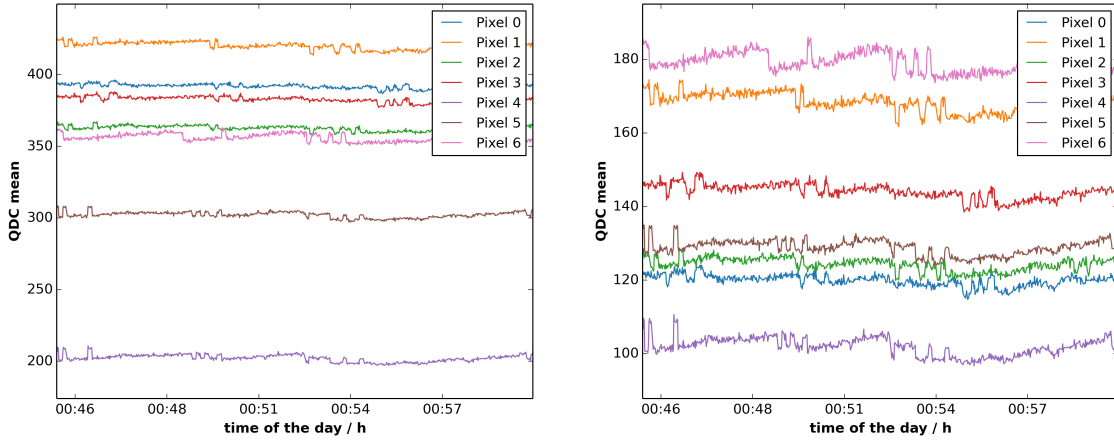


Figure 5.5: Visualization of the benefit of the calibration of the SiPMs pedestal. Left: measurement in darkness without calibration of the pedestal. Right: calibration of the pedestal is applied to the former measurement. The distance between the individual pixels has decreased considerably.

spacing between the individual pixels decreases considerably. The remaining differences are due to a varying dark rate or a varying of the gain between the pixels.

5.3 Focusing of the FAMOUS camera

The great challenge in the process of focusing is, that the telescope should be focused to infinity. Within his master thesis, Hans Michael Eichler has studied the characteristics of the optics of the FAMOUS telescope [26]. He determined the best focal length for the FAMOUS prototype to 505-507 mm. The selection of this focal distance achieved the best compromise of best sharpness for all possible angles of entrance.

In the workshop of III. Physikalisches Institut A, RWTH Aachen, the distance between backplane of the Fresnel lens and the entrance of the Winston Cones is adjusted to 506.56 mm.

Measurements

During this bachelor thesis, several measurements have been performed to test the behavior of the telescope electric and the data acquisition system. This leads to the discovery of some necessary improvements. These are discussed in the following section. The results of the performed measurements are presented as well.

6.1 Discovered necessary improvements

As the FAMOUS telescope is a prototype, its main aim is to detect sources of errors, which had not been considered during the construction.

The first obvious problem in an outside measurement is the fog of the Fresnel lens. In figure 6.1 the effect becomes obvious. To deal with this problem in the short term, the measurements were performed upon the air condition of the Physikzentrum, RWTH Aachen. In the long term, a ventilation system or a heating for the optics has to be developed. This is currently under consideration.

Another more hidden problem is an oscillation of the bias voltage supplied by the FTFC, which is only partly compensated by the following electric. Thus the over voltage is not stable and oscillates as well in some range. The precise effects and the issue are currently under investigation.

The desired distance of time between two measurements is five seconds. Due to the superposition of processes in the data acquisition, some measurements are performed with a much shorter distance of time. There are already methods to avoid this behavior, but it is not detected immediately every time. An software update will avoid the concurrent activity of more than one measurement process.

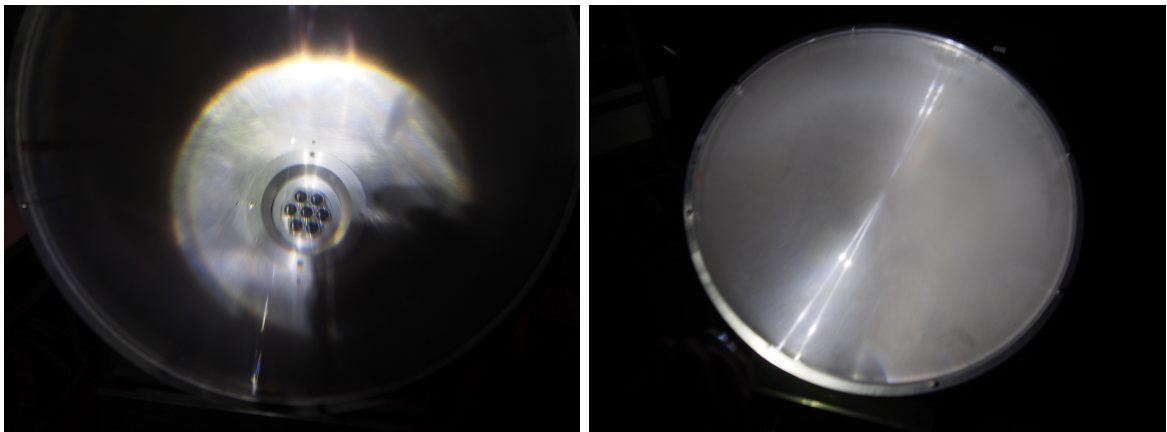


Figure 6.1: Left: not fogged optics. Right: fogged optics. Both pictures are taken under the same light conditions. Taken from [44].

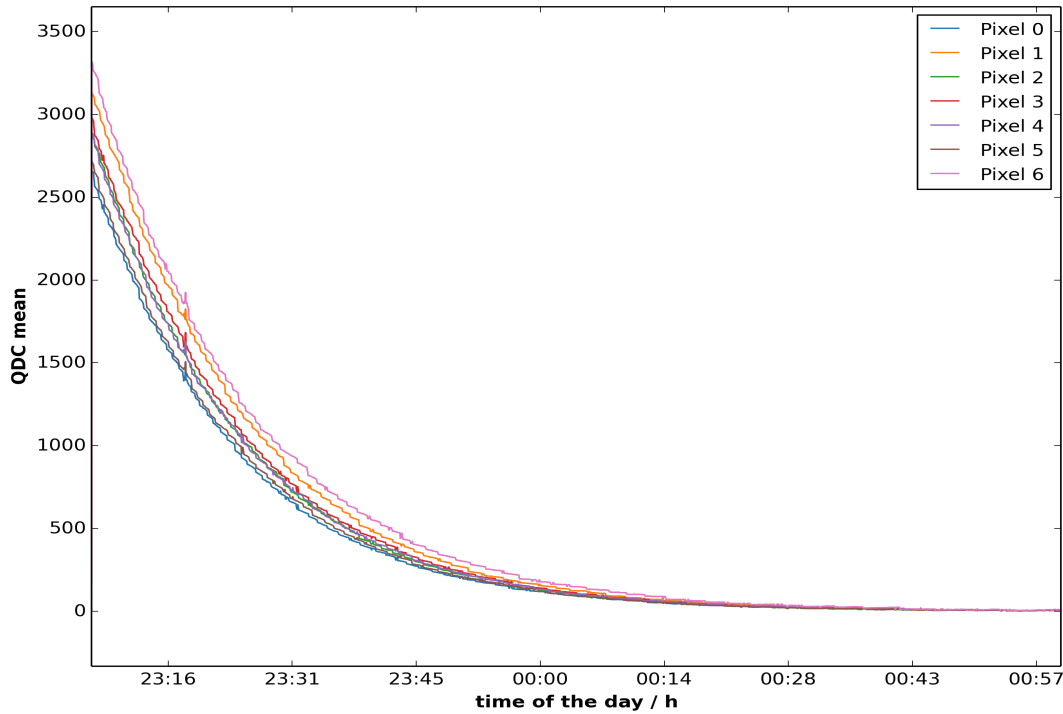


Figure 6.2: Measurement during dawn performed 23 and 24.06.2014. The over voltage was set to 1 V. The behavior of the individual pixels are alike to each other. The short increase of the signal at approximately 23:20 is a car which headlights were directed towards FAMOUS. For better visibility, the minimum for all pixels has been set to zero.

6.2 Measurements during dawn

In the previous chapter, in section 5.1, several methods to determine the over voltage have been presented. These are later compared to the recommended bias voltage provided by Hamamatsu. To test these recommended values, the behavior of the QDC signal is recorded during the dawn from 23. to 24. July 2014 (c.f. figure 6.2). The behavior of the individual pixels is sufficiently comparable to each other. The slightly different slopes of the signals shows an minor gain variation.

6.3 Night sky brightness

For the investigation of the emitted fluorescence light by extensive air showers, the background brightness is a critical parameter. For a high efficiency in the distinction between background and air shower, the ambient light should be as low as possible.

Since the light pollution is not negligibly, Aachen is not the best place for the observation of extensive air showers. To study the light pollution as well as the influence of the lunar cycle, background measurements have been performed in three different nights. After the offset correction is performed (c.f. 5.2), the average out of the individual

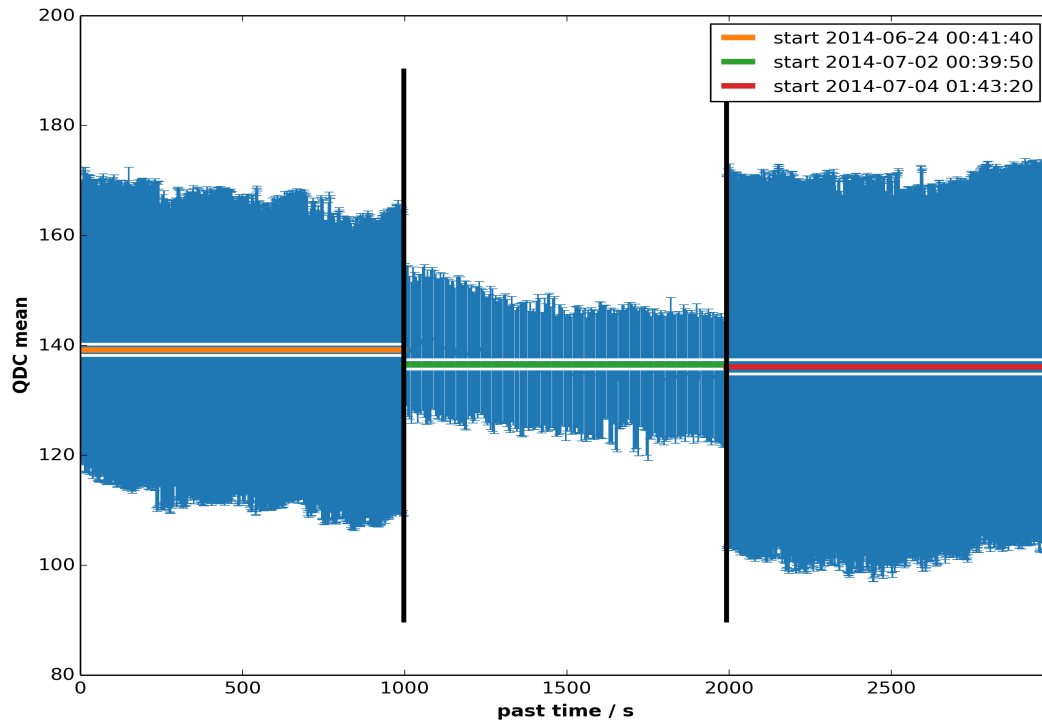


Figure 6.3: Study of the night sky brightness for three different nights. FAMOUS is adjusted to an area nearly empty of stars and as close to the zenith as possible. The moon was not in the sky during the measurements. On the y-axis, the average of the QDC values of all pixel is calculated. The lines represents the average of the measurement. The white lines representing the one sigma are. The different sizes of the errors is due to an unwanted superposition in the DAQ.

pixels is calculated. FAMOUS is oriented to an area nearly empty of visible stars and as close to the zenith as possible. The actual design allows an angle of approximately 72° to the horizontal. At this position, a measurement for 1000s is performed. The moon was not in the sky during the measurements, because he has set down before or has not yet risen. Beside this, the fraction of the moon variates from 11 % for the 24.06 to 19 % at 02.07 and 36 % at 04.07.

By use of equation 4.7 and 4.8 the average and the estimator for the standard deviation is calculated for each time. For each run on a date the weighted average is calculated as well. The result of the measurement is presented in figure 6.3. In this figure, the discussed superposition in the DAQ becomes visible. It appeared for the 24.06.14 and 04.07.14 and might be an factor for the variation of the relative errors.

The night sky brightness is not only characterized by a daily fluctuation but also has an angular dependency. To study these, the following measurement is performed. Starting in the maximum possible angle to the horizontal, the angle is reduced in steps of approximately ten degrees. For each angular adjustment, a measurement lasting approximately five minutes is progressed. The direction of view is chosen that as less

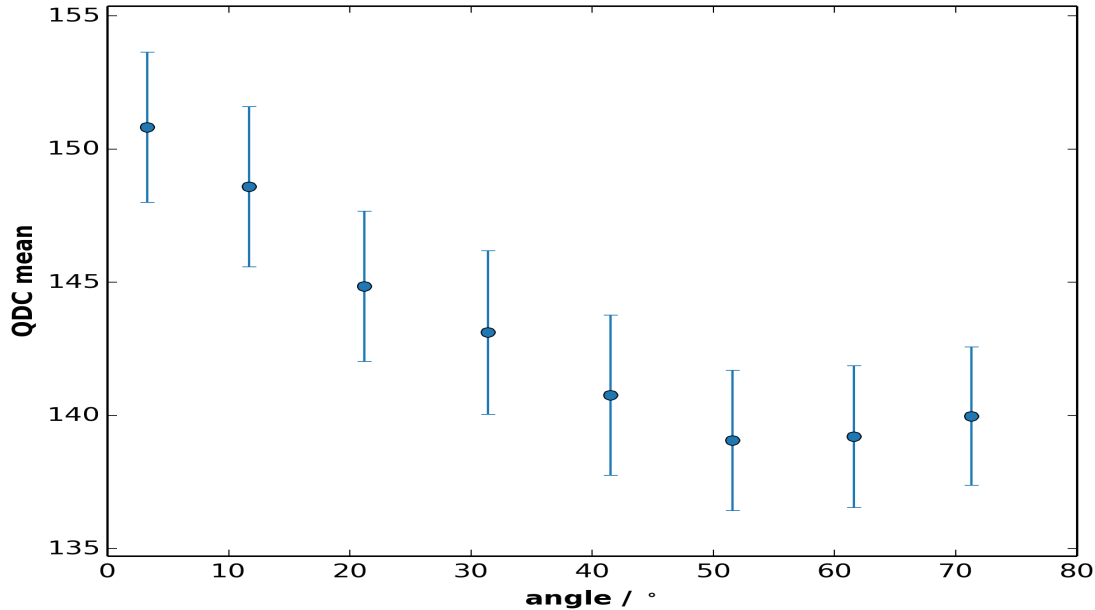


Figure 6.4: Angular dependency of the night sky brightness. The data points represents the error weighted average for angle (c.f. figure 6.3), especially because the m. The signal of the 4. pixel is neglected for the evaluation, since the connection to the pixel has lost during the measurement. The direction of viewing is chosen, in that way, that as few as possible nearby light sources affect the measurement.

near light sources are in the direct field of view as possible. The performed measurement is analyzed by use of equation 4.7 and 4.8 as well. The result is the weighted average for each angular adjustment. Unfortunately, the connection for the 4. pixel has been lost during the measurement, since a plug has been drawn out. This pixel is neglected in the analyses. As seen in figure 6.4 the brightness decreases from horizon to zenith. This is due to the decreasing light pollution.

6.4 Traces of celestial objects

In several nights, the passage of celestial objects has been recorded with the Famous telescope. These measurements are presented in this section.

6.4.1 Trace of the moon

During the night from 6. to 7. June, the passage of the moon through the field of view of the FAMOUS telescope has been recorded with an over voltage of 0.7 V. The results are presented in figure 6.5. On the top of the figure, the traces recorded for the individual pixels can be found. An offset correction has been performed, in which the minimum QDC value of all traces has been set to zero. The effect of the saturation of the QDC becomes clearly visible. The different levels of the saturation are an effect of the offset correction. The behavior of the curves, especially the abrupt changes of the levels in all pixels is due to clouds which have moved in front of the moon. This development is also detected via the SkyCam (c.f. 6.6).

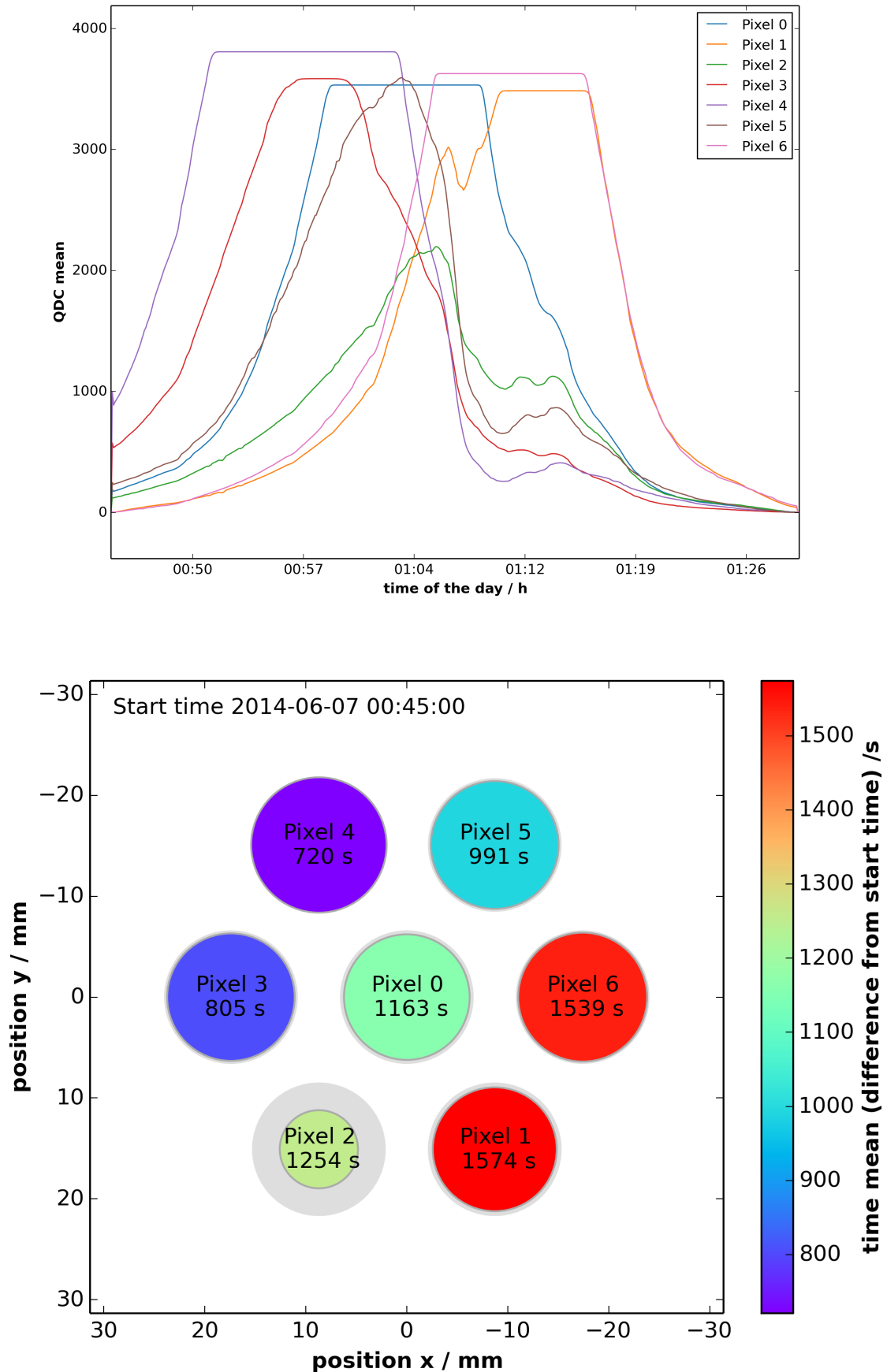


Figure 6.5: Trace of the moon performed at 06.07.14 with 0.7 V over voltage. Up: plot of the QDC Measurement. The minimum of each pixel has been set to zero. The cut of for high qdc values is a result of saturation of the QDC. Down: visualization of the trace of the star. The mean of time weighted by the QDC value is color coded. The maximum radius symbolizes the maximal occurring QDC value.



Figure 6.6: SkyCam images for the passage of the moon. The images are taken from 0:45 (top left) to 1:30 (down right). The field of view of the image equals the field of view of the FAMOUS telescope.

To evaluate the recorded traces, the following method has been developed. The aim is the calculation of the point when the moon or an other celestial object is mostly measured by a pixel. To achieve this, the average of time is calculated, weighted by the individual QDC value. In order to not affect the calculation by long time spans without any object in the field of views, only values with a QDC value grater than a specific threshold are used. In case of this measurement, the threshold is set to a QDC value of 1000. The calculated average times can be found as a color code in the lower image in figure 6.5. This image is a sketch of the FAMOUS camera. The orientation of the axes are laid out in such a manner that the orientation equals a view into the sky from a person standing behind FAMOUS. The spacing size of the pixel in the image is true to scale. Whereas radius of the colored circle signifying the maximum measured value for each pixel.

6.4.2 Traces of stars

Beside the detection of the moon the question occurs, if also stars can be detected by the FAMOUS telescope. This could be verified using the example of the star Arcturus and an over voltage of 1 V. In figure 6.7 an example of these measurements can be found. In contrast to 6.5 the saturation of the QDC does not affect the data acquisition. In exchange for that, an oscillation of the QDC values can be discovered. Among fluctuations in the atmosphere, this oscillations is a result of the oscillation in the FTFC. In order to compensate these fluctuations, a moving average over three values is calculated. The following evaluation of the traces is equal to section 6.4.1, whereas the threshold has set to a QDC value of 20.

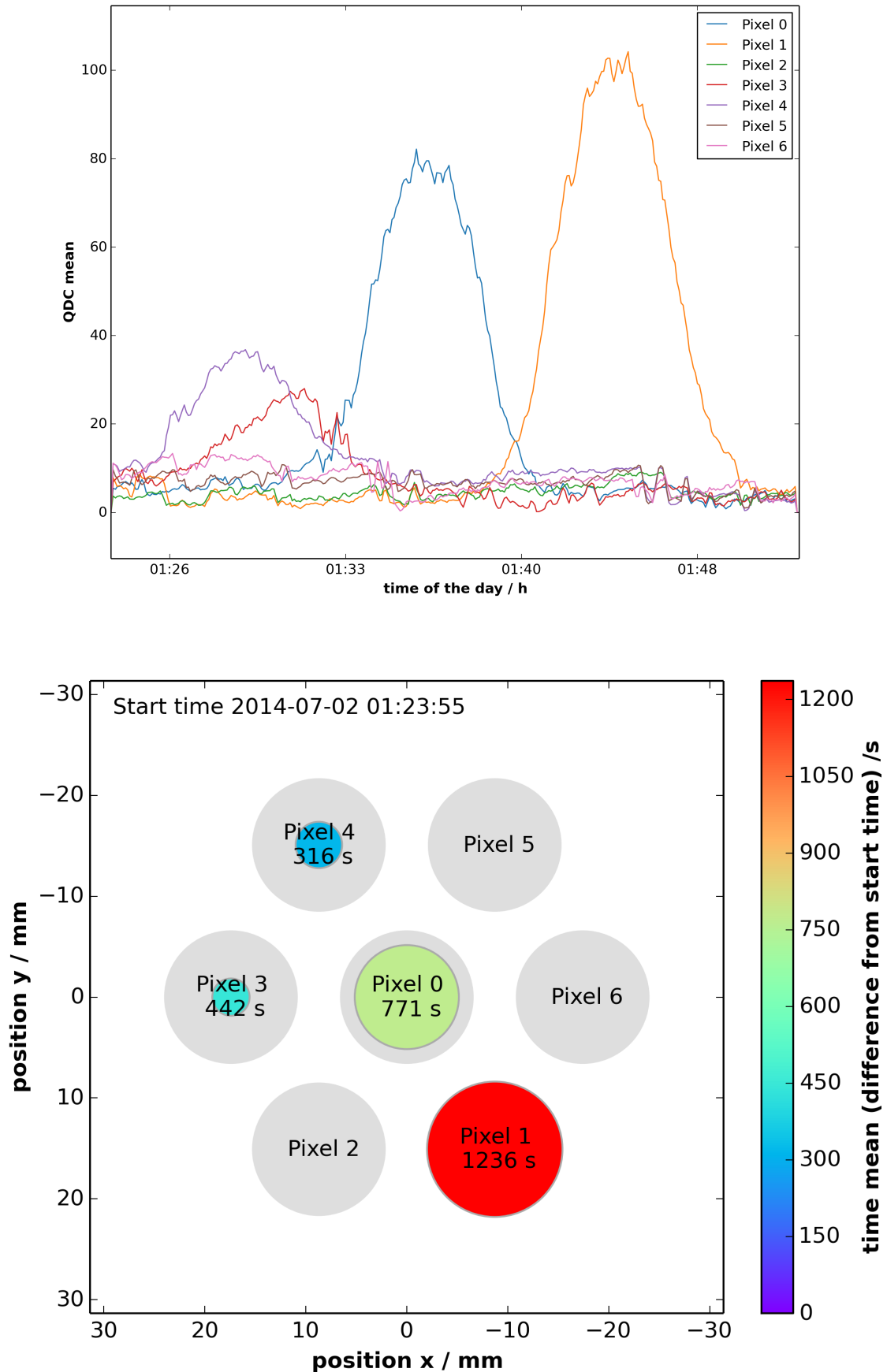


Figure 6.7: Trace of Arcturus performed at 03.07.14 with 1 V over voltage. Up: plot of the QDC Measurement including a moving average over 3 value. The minimum of each pixel has been set to zero. Down: visualization of the trace of the star. The mean of time weighted by the QDC value is color coded. The maximum radius symbolizes the maximal occurring qdc value.

Summary and Outlook

The observation of ultra high energy cosmic rays is a great field of research. The Pierre Auger Observatory has been developed as a hybrid detector for this purpose, consisting of a surface and a fluorescence detector. In the current status of the observatory photomultiplier tubes (PMTs) are used as the detector component in the cameras of the fluorescence detector.

Silicon photomultipliers (SiPMs) are a promising technique for the replacement of PMTs and the performance of single photo counting. They have excellent features like a low required bias voltage and a compact design.

In III. Physikalisches Institut, RWTH Aachen, a SiPM based telescope has been developed. The acronym stands for „**F**irst **A**uger **M**ulti-pixel photon counter camera for the **O**bservation of **U**ltra-high-energy air **S**howers“. Within this thesis, the commissioning of the FAMOUS telescope have been carried out successfully. As well, initial nightly measurements have been performed.

As the sensitive detector component of the telescope are silicon photomultipliers, the determination of the breakdown voltage V_{break} is of great importance. In this thesis, three different methods for the determination of V_{break} have been presented. Two of them are based on the finger like charge spectrum, which is not needed by the third. This one enables a simple and still reliable calibration of V_{break} . With help of the the different methods, the values as specified by the manufacturer Hamamatsu could be reproduced successfully.

In the nearer future, the use of a pulsed LED will promises a further improvement of the methods, which are based on the finger spectrum.

Within the commissioning, the focusing of the FAMOUS camera as well as the calibration of the pedestal of the SiPMs has been accomplished.

The SkyCam module, which has been implemented in this thesis enables the automatic detection and identification of stars in the field of view of FAMOUS.

The SkyCam itself is a CMOS camera combined with a lens with a focal length of $f = 8.5$ mm. For the correction of the image distortion, a method based on the OpenCV package has been developed. Also a test of robustness in dependence on several parameters has been performed. The observed parameters are focal ratio, viewing angle and operation mode of the camera (monochrome or color).

On the basis of the Astrometry.net software, a routine has been developed, which enables the autonomous scanning of the sky. The routine includes an automatic adjustment of the exposure and the analysis of the taken images. Over the course of several measurements, the implementation has been proven to be robust.

In a further step, the SkyCam analysis of the data could be improved, to allow the determination of the abundances of aerosols in the atmosphere. This could be achieved by the comparison of the measured brightnesses of stars and the comparison to their cataloged values. Another benefit of such an upgrade would be the possibility of the determination of the cloud coverage.

Furthermore, several measurements during night have been performed with the FAMOUS telescope prototype. The traces of celestial objects like the moon and Arcturus could be recorded. Furthermore, the variation of the night sky brightness in subject to the viewing angle and in course of several nights has been studied.

During these measurements, some issues and necessarily improvements of the electronics and the telescope construction have been discovered. The solution approaches have been discussed as well. For the 64 pixel version of the telescope, the elimination of these issues will improve the performance of measurements. Thus the proof of principle for the detection of cosmic rays with help of the FAMOUS telescope is can be brought forward in the near future.

References

- [1] FAMOUS GROUP OF THE PIERRE AUGER COLLABORATION, *FAMOUS slow control website, dashboard*, June 2014.
- [2] J. BLUEMER, R. ENGEL, AND J. R. HOERANDEL, *Cosmic rays from the knee to the highest energies*, (2009). arXiv: 0904.0725.
- [3] P. AUGER *et al.*, *Extensive cosmic-ray showers*, Reviews of Modern Physics, (1939).
- [4] H. TAJIMA, *Detectors for cosmic rays on ground and in space*, (2007). arXiv: 0709.0634.
- [5] J. BERINGER *et al.*, *Review of particle physics*, Physical Review D, 86 (2012).
- [6] K.-H. KAMPERT AND P. TINYAKOV, *Cosmic rays from the ankle to the cut-off*, Comptes Rendus Physique, (2014). arXiv: 1405.0575.
- [7] A. ERLYKIN AND A. WOLFENDALE, *Structures in the cosmic ray energy spectra*, (2013). arXiv: 1310.3076.
- [8] B. G. KEILHAUER, *Investigation of Atmospheric Effects on the Development of Extensive Air Showers and their Detection with the Pierre Auger Observatory*, PhD thesis, Universität Karlsruhe (TH), Karlsruhe, 2004.
- [9] W. HEITLER, *The quantum theory of radiation*, Oxford University Press, 1947.
- [10] M. UNGER *et al.*, *Reconstruction of longitudinal profiles of ultra-high energy cosmic ray showers from fluorescence and cherenkov light measurements*, (2008). arXiv: 0801.4309.
- [11] THE PIERRE AUGER COLLABORATION *et al.*, *The fluorescence detector of the Pierre Auger Observatory*, (2010). arXiv: 0907.4282.
- [12] F. ARQUEROS, J. R. HOERANDEL, AND B. KEILHAUER, *Air fluorescence relevant for cosmic-ray detection - summary of the 5th fluorescence workshop, el escorial 2007*, (2008). arXiv: 0807.3760.
- [13] THE PIERRE AUGER COLLABORATION , *Pierre Auger Observatory*, <http://auger.org>, June 2014.
- [14] I. ALLEKOTTE *et al.*, *The surface detector system of the Pierre Auger Observatory*, (2008). arXiv: 0712.2832.
- [15] N. DINU, *Instrumentation on Silicon Detectors: from properties characterization to applications*, PhD thesis, Université Paris Sud-Paris XI, 2013.
- [16] D. RENKER AND E. LORENZ, *Advances in solid state photon detectors*, (2009).

-
- [17] J. RENNEFELD, *Studien zur Eignung für den Einsatz von Silizium Photomultipliern für den Einsatz im erweiterten CMS Detektor am SLHC*, diploma thesis, III. Physikalisches Institut B, RWTH Aachen, 2010.
- [18] M. STEPHAN *et al.*, INTERNATIONAL SOCIETY FOR OPTICS AND PHOTONICS, *Future use of silicon photomultipliers for the fluorescence detection of ultra-high-energy cosmic rays*, in SPIE Optical Engineering+ Applications, 2011.
- [19] HAMAMATSU, *Product information MPPC S10984/S10985 series*, June 2014.
- [20] J. SCHUMACHER, *Characterization studies of silicon photomultipliers: Noise and relative photon detection efficiency*, bachelor thesis, III. Physikalisches Institut A, RWTH Aachen University, 2013.
- [21] M. LAUSCHER, *Characterisation studies of silicon photomultipliers for the detection of fluorescence light from extensive air showers*, master thesis, III. Physikalisches Institut A, RWTH Aachen University, 2012.
- [22] T. NIGGEMANN *et al.*, *Status of the silicon photomultiplier telescope FAMOUS for the fluorescence detection of UHECRs*.
- [23] HAMAMATSU, *Product information MPPC S12571-015C*, June 2014.
- [24] C. PETERS, *Design studies for an air fluorescence telescope with silicon photomultipliers for the detection of ultra-high-energy cosmic rays*, master thesis, III. Physikalisches Institut A, RWTH Aachen University, 2013.
- [25] M. STEPHAN *et al.*, EDP SCIENCES, *FAMOUS—a prototype silicon photomultiplier telescope for the fluorescence detection of ultra-high-energy cosmic rays*, in EPJ Web of Conferences, 2013.
- [26] H. M. EICHLER, *Characterisation studies on the optics of the prototype fluorescence telescope FAMOUS*, master thesis, III. Physikalisches Institut A, RWTH Aachen University, 2014.
- [27] R. WINSTON, J. C. MIÑANO, AND P. BENITEZ, *Nonimaging optics*, Academic Press, 2005.
- [28] S. MANN, *Measurement of the uv reflectivity of aluminium in different stages of oxidation*, bachelor thesis, III. Physikalisches Institut A, RWTH Aachen University, 2012.
- [29] SCHOTT, *Product information UV-pass filter UG-11*, June 2014.
- [30] CAEN, ELECTRONIC INSTRUMENTARION, *Product information for QDC model V965*, June 2014.
- [31] WIENER, PLEIN & BAUS ELEKTRONIK, *Product information for VM-USB VME Controller*, June 2014.
- [32] INTEL, *Product information for Mini-PC-Intel NUC-Kit D54250WYK*, June 2014.

-
- [33] J. GROTHOFF, *Development of a data acquisition system for the air shower fluorescence telescope famous*, bachelor thesis, III. Physikalisches Institut A, RWTH Aachen University, 2013.
 - [34] ASTROLUMINA, *Alccd-QHY-5L-II product information*, June 2014.
 - [35] EDMUND OPTICS, *Techspec compact fixed focal length lens product 58-000 information*, June 2014.
 - [36] OPENCV, *Camera calibration with OpenCV*, June 2014.
 - [37] OPENCV, *Camera calibration and 3D reconstruction*, June 2014.
 - [38] W. DEMTRÖDER, *Experimentalphysik 2: Elektrizität und Optik*, Springer, 2013.
 - [39] M. ERDMANN AND T. HEBBEKER, *Experimental-physik 5*, Springer, 2013.
 - [40] B. E. BAYER, *Color imaging array*, July 20 1976. US Patent 3,971,065.
 - [41] D. W. HOOG *et al.*, *Astrometry.net*, <http://astrometry.net>, June 2014.
 - [42] S. ROWEIS *et al.*, *Making the sky searchable: Fast geometric hashing for automated astrometry*, June 2014.
 - [43] III. PHYSIKALISCHES INSTITUT A, RWTH AACHEN UNIVERSITY, *Bedingungsanleitung Universalpulser V2*, Apr. 2013.
 - [44] M. SCHAUFEL, „private communications“.

Acknowledgements

Während dem Entstehungsprozess dieser Arbeit haben mich viele unterstützt und begleitet. An dieser Stelle möchte ich mich gerne herzlichst bei ihnen allen bedanken. Ohne ihre Hilfe wäre diese Arbeit so nicht möglich gewesen.

Zuerst möchte ich Prof. Dr. Hebbeker danken, dass er mir die Möglichkeit gegeben hat an solch einem spannenden Projekt mitzuarbeiten. Gleichzeitig konnte ich dadurch erste Einblicke in aktuelle Forschungsarbeit gewinnen.

Darüber hinaus möchte ich besonders meinem Betreuer Tim Niggemann danken, an den ich mich mit allen Problemen wenden konnte. Auch bei der gesamten Auger Arbeitsgruppe möchte ich mich bedanken. Zum einen dafür, dass ich sie immer um Rat fragen konnte, zum anderen für das wunderbare Arbeitsklima. Gleiches gilt meine beiden Bürokollegen Markus Wirtz und Dominik Sommer. Vielen Dank für das entspannte Klima in unserem Büro.

Auch möchte ich Merlin Schaufel danken, das wir uns gegenseitig beim Umgang mit FAMOUS unterstützt haben. Seine vielen, oft kreativen Ideen haben mir sehr weitergeholfen.

Zuletzt möchte ich meiner Familie und meinen Freunden danken für den Rückhalt und die Unterstützung während dieser Zeit.

Erklärung

Hiermit versichere ich, dass ich diese Arbeit einschließlich beigefügter Zeichnungen, Darstellungen und Tabellen selbstständig angefertigt und keine anderen als die angegebenen Hilfsmittel und Quellen verwendet habe. Alle Stellen, die dem Wortlaut oder dem Sinn nach anderen Werken entnommen sind, habe ich in jedem einzelnen Fall unter genauer Angabe der Quelle deutlich als Entlehnung kenntlich gemacht.

Aachen, den 21. Juli 2014

Franziska Hanna Knuth

